

See discussions, stats, and author profiles for this publication at: <https://www.researchgate.net/publication/251415702>

Monazite-Xenotime-Garnet Equilibrium in Metapelites and a New Monazite-Garnet Thermometer

Article · January 2001

DOI: 10.1093/petrology/42.11.2083

CITATIONS

264

READS

109

3 authors, including:



Joseph M. Pyle

Bechtel Marine Propulsion Corporation

35 PUBLICATIONS **1,923** CITATIONS

[SEE PROFILE](#)



Roberta L. Rudnick

University of California, Santa Barbara

240 PUBLICATIONS **20,588** CITATIONS

[SEE PROFILE](#)

Some of the authors of this publication are also working on these related projects:



Tracing continental weathering using lithium isotopes [View project](#)



Structure and Composition of the Continental Crust from EarthScope USArray [View project](#)

Monazite–Xenotime–Garnet Equilibrium in Metapelites and a New Monazite–Garnet Thermometer

JOSEPH M. PYLE^{1*}, FRANK S. SPEAR¹, ROBERTA L. RUDNICK^{2†}
AND WILLIAM F. McDONOUGH^{2†}

¹DEPARTMENT OF EARTH AND ENVIRONMENTAL SCIENCES, RENSSELAER POLYTECHNIC INSTITUTE, TROY, NY 12180, USA

²DEPARTMENT OF EARTH AND PLANETARY SCIENCES, HARVARD UNIVERSITY, CAMBRIDGE, MA 01238, USA

RECEIVED AUGUST 15, 2000; REVISED TYPESCRIPT ACCEPTED MAY 8, 2001

Prograde suites of pelitic rocks were examined with electron microprobe and laser ablation inductively coupled plasma mass spectrometry to determine the systematics of element partitioning between coexisting monazite, xenotime, and garnet. Monazite grains that grew in equilibrium with xenotime are enriched in Y and Dy compared with monazite that grew in xenotime-absent assemblages. Y and heavy rare earth element contents of monazite coexisting with xenotime increase with rising temperature. Monazite–xenotime Y–Gd and Y–Dy partitioning is systematic within a metamorphic grade, and increases slightly with increasing metamorphic grade, suggesting that monazite–xenotime pairs approached partitioning equilibrium. Garnet and monazite in both xenotime-bearing and xenotime-absent assemblages show a strong ($R^2 = 0.94$) systematic relationship between inverse temperature and $\ln(K_{Eq})$ for the net-transfer equilibrium $YAG + OH\text{-}Ap + (25/4)Qtz = (5/4)Grs + (5/4)An + 3YPO_4\text{-}Mnz + 1/2H_2O$, suggesting that garnet and monazite crystallized in compositional equilibrium. The following temperature– K_{Eq} relationship for the equilibrium above has been derived:

$$T(^{\circ}C) = \left[\frac{-1.45P(\text{bars}) + 447772(\pm 32052)}{567(\pm 40) - R\ln(K_{Eq})} \right] - 273.15$$

with a precision of some $\pm 30^{\circ}C$ for temperature estimates. Our observations suggest that major and accessory phases interact in a coupled fashion during metamorphism, and also approach a state of compositional equilibrium as reactions proceed.

KEY WORDS: garnet; monazite; partitioning; thermometry; xenotime

INTRODUCTION

Monazite $[(Ce,La,Th)PO_4]$ plays an important role in studies of igneous and metamorphic petrogenesis. Foremost, monazite is used to date specific events in a petrogenetic sequence (e.g. Parrish, 1990; Harrison *et al.*, 1997; Hawkins & Bowring, 1999; Foster *et al.*, 2000). Monazite may contain a large percentage of the sample rare earth element (REE) budget and, thus, exert an important influence on the evolution of melt composition (Wark & Miller, 1993; Bea, 1996). The thermobarometric potential of monazite (coexisting with xenotime) has been recognized, leading to calibration of monazite geothermometers (Gratz & Heinrich, 1997, 1998; Heinrich *et al.*, 1997; Andrehs & Heinrich, 1998). In addition, the recognition that nearly all lead in monazite is radiogenic (Parrish, 1990; Montel *et al.*, 1994) has led to development and application of electron microprobe monazite dating techniques (Suzuki & Adachi, 1991; Montel *et al.*, 1996; Williams *et al.*, 1999).

Full realization of monazite as a thermochronometer requires detailed understanding of the specific reactions responsible for its formation. Previous studies of monazite petrogenesis have focused on monazite compositional zonation (Zhu & O'Nions, 1999a, 1999b), monazite growth kinetics (Ayers *et al.*, 1999), behavior of monazite during hydrothermal alteration (Poitrasson *et al.*, 1996; Crowley & Ghent, 1999) and melting events (Watt, 1995), or, to a limited extent, the influence of major-phase mineral assemblage in monazite reactivity (Zhu &

*Corresponding author. Telephone: (518) 276-4899. Fax: (518) 276-6680. E-mail: pylej@rpi.edu

†Present address: Department of Geology, University of Maryland, College Park, MD 20742, USA.

O'Nions, 1999b). Textural relationships between monazite and other accessory phases (allanite, apatite, epidote, titanite) indicate that monazite is involved in reaction relationships with other REE-accessory minerals (Broska & Siman; 1998; Finger *et al.*, 1998), but only a limited number of studies address specific reactions responsible for formation of metamorphic monazite (Bingen *et al.*, 1996; Pan, 1997; Ferry, 2000).

This paper focuses on monazite, xenotime, garnet, and, to a lesser extent, apatite because (1) they are significant geochronometers, (2) a large portion of a typical pelite REE and Y budget is contained in these phases, and (3) zoning in garnet and monazite record significant details of the reaction history. We attempt to demonstrate that metamorphic monazite approaches compositional equilibrium with both coexisting major and accessory phases. Moreover, we present element partitioning data for coexisting monazite, xenotime, and garnet that support the interpretation of an approach to compositional equilibrium between and among these minerals—a critical step in the process of identifying specific reactions responsible for the formation and destruction of metamorphic monazite. Finally, we demonstrate the utility of Y partitioning between garnet and monazite as a potential thermometer.

SAMPLE AND ANALYTICAL PROCEDURES

Twenty-eight pelites with well-characterized P - T histories from three localities (Table 1) were chosen for study. The samples are the same as those studied by Pyle & Spear (1999), and field area details have been given therein. Additional information on the samples examined in this study has been given by Spear *et al.* (1990, 1995), Spear (1992), Kohn *et al.* (1993, 1997), Menard & Spear (1993, 1994), Spear & Kohn (1996), and Spear & Parrish (1996).

Details of image acquisition, element map generation, and quantitative electron microprobe (EMP) analysis of garnet have been given by Pyle & Spear (1999). X-ray maps were obtained and analyses were performed on a JEOL 733 Superprobe at Rensselaer Polytechnic Institute. For monazite element maps we used a 15 kV accelerating voltage, beam current of ~ 150 nA, map step size of $1\text{--}2\text{ }\mu\text{m}/\text{pixel}$, and dwell times of $30\text{--}50$ ms/pixel. For quantitative spot analysis of monazite and xenotime, a combination of natural and synthetic phosphate, silicate, and oxide standards was used (Table 2), with an accelerating voltage of 15 kV, beam current of ~ 50 nA, and counting times of 30 s each on peak and background. The ZAF matrix correction used was that of Armstrong (1984). Selected monazite and xenotime

grains (Tables 4 and 5) were reanalyzed at longer counting times and higher current (120 s, 100 nA) to improve detection limits. Minimum detection limit (MDL) is calculated using the relationship from Ziebold (1967), $\text{MDL} \geq 3.29 C_{\text{std}} / (P^2/B)^{1/2}$, where C_{std} is the weight per cent of the element of interest in the standard, P equals the total number of peak-background counts, and B equals the total number of background counts. In Table 2, 12 000 nA s detection limits for REE, Y, U, Pb, and Th are listed. Analyses listed in Tables 4 and 5 are single-spot analyses.

Quantitative analysis of REE phosphate generally requires some correction because of interference of overlapping characteristic X-ray peaks (Scherrer *et al.*, 2000). Off-line corrections for interferences were made to the following elements (Table 3): P, U, Pb, Nd, Gd, Er. For monazite compositions in this study ($0.0\text{--}9.5$ wt % ThO_2), Th interference ($\text{M2-O4} + \text{M}\zeta 1$ and $\text{M}\zeta 2$) on Pb ($\text{M}\alpha$) is minor (≤ 120 ppm apparent PbO from ThO_2 interference) and is ignored. Interfering X-ray lines and correction factors are given in Table 3. Empirical correction factors calculated in this way broadly agree with correction factors calculated using the program Virtual WDS (Reed & Buckley, 1996; see also Scherrer *et al.*, 2000).

Quantitative EMP analysis of apatite is hindered by F excitation phenomena (Stormer *et al.*, 1993). Prioritization of F analysis, $10\text{ }\mu\text{m}$ spot size, low current (~ 20 nA on the Faraday cup) and short counting times (15 s on peak) were used to minimize F excitation. Repeated analyses on the same spot of Durango apatite using the above analysis schedule demonstrated F volatilization, but no apparent increase in F concentration. Repeated analyses on different spots of the Durango apatite standard gave an average value of 3.42 ± 0.11 (1σ) wt % F ($n = 21$).

Major silicate phases from 11 of the 28 samples were analyzed for REE, U, Pb, and Th using the laser ablation inductively coupled plasma mass spectrometry (LA-ICP-MS) system at the Department of Earth and Planetary Sciences, Harvard University. Samples were ablated using an excimer laser (Lambda Physik), which produces a 193 nm laser light with a 15 ns pulse duration. Spot size varied between $35\text{ }\mu\text{m}$ (for small grains) and $90\text{ }\mu\text{m}$ (for large grains) in diameter; ablated grains were typically between 500 and $20\,000\text{ }\mu\text{m}$ in diameter, resulting in ablation percentages (on an area basis) of $0.002\text{--}0.5\%$. The ablated material was analyzed in fast peak hopping mode with a PQ II+ quadrupole ICP-MS (VG-Elemental) system. Each analysis incorporated a background acquisition of ~ 60 s, with total acquisition times varying between 120 and 240 s. Factory-supplied software was utilized in the acquisition of individual time-resolved analyses. Details of acquisition and calculation of transient signals have been described by Longerich *et al.* (1996). External calibration was performed relative to NIST 610

Table 1: Sample grade and accessory mineral assemblage

Sample	Grade	Mon	Ap	Zrn	Ilm	Fe-sulfide	Xen	Other
<i>Eastern Vermont terrane, Bronson Hill terrane, Merrimack terrane, S. Vermont–New Hampshire, USA</i>								
BF-55A	Bt–Chl	m		X		X	m	Rt, britholite (?)
BF-55B	Bt–Chl	m	X	X		X	m	Rt, florencite
BF-56A	Bt–Chl	m	X	X		X	m	Cc, Rt
BF-53	Grt	m	X	X	X		m	thorite(?)
BF-15A	Grt	m	X	X	X		m	
PUT-92C2	Grt	m	X	X	X	X		
93–19A	Grt	m	X	X	X	X	m, r	Ccp, Sp, Rt
BF-17A	St	m	X	X		X	i	Gr, Rt
BF-18C	St	m	X	X	X	X	r?	
BF-38B1B	St	m	X	X	X		i	Rt
BF-52A	St	m	X	X	X	X	r	Rt
BF-57B	St	m, i	X	X	X	X	r?	Sp
BF-58B	St	m, i	X	X	X			
BF-64	St	m	X	X	X	X	r	Rt
BF-92B	St–Ky	m, i	X	X	X		i	
89–9	Sil	m	X	X	X	X	i	Rt, Gr
89–22	Sil	m, i	X	X	X		i	
BF-78	Sil	m, i	X	X	X	X	i	
BF-14P	Mig	m, i	X	X	X		i, r, m	Spl
LM-1A2	Mig	m, i	X	X	X	X	i, m	Rt, Ccp
<i>Eastern Vermont terrane, east-central Vermont, USA</i>								
TM-549	Grt	m	X	X	X		i	Tur, Rt, Ank
TM-445	St	m	X	X	X		m	Aln, Ep, Ttn, Gr, Mt
TM-637	St–Ky	m	X	X	X		m	Ep, Gr, Tur
<i>Valhalla complex, southern British Columbia, Canada</i>								
V6A	Mig	m, i	X	X	X			Rt
V6B	Mig	m, i		X	X	X	i, m	Rt
V7C	Mig	m, i	X	X	X			Rt
V7D	Mig	m, i	X	X	X	X	m	Rt
<i>Cordillera Darwin complex, Tierra Del Fuego, Chile</i>								
SP-9B1	St–Ky	X	X	X	X		m	Ep, Rt

X, mineral identified in sample; i, xenotime or monazite present as inclusion in garnet; m, xenotime or monazite present as matrix phase; r, xenotime or monazite present in reaction zone in or around garnet (distinction for xenotime only); ?, tentative identification only. Mineral abbreviations after Kretz (1983), with additional from Pyle & Spear (1999).

and ^{43}Ca was used as an internal standard. Barth *et al.* (2001) reported values assumed for NIST 610 as well as analyses of the BIR-1G and BCR-2G glass standards. The time-resolved spectra were processed off-line using a modified version of the program LAMTRACE (coded by Simon Jackson). Further details of laser and ICP-MS setup and operating conditions have been given by Horn *et al.* (2000). Analyses generally consist of two spots per grain; exceptions are noted in Table 6. Where

appropriate, the standard deviation of multiple analyses is given in parentheses.

RESULTS

Monazite and xenotime compositions

Representative analyses of xenotime and monazite are given in Tables 4 and 5. All point analyses with 97 <

Table 2: Analysis setup and operating conditions for xenotime and monazite EMP analyses

Element	Line	Std.	Crystal	Bkg high	Bkg low (−Δmm)	Bias (V)	Baseline (V)	Window (V)	Detection limit (ppm)
Ca	Kα1	apatite	PET	1.0	2.0	1700	1.5	5.0	75
P	Kα1	CePO ₄	TAP	5.0	−5.0*	1700	0.8	3.2	330
Si	Kα1	ThSiO ₄	TAP	3.5	2.9	1700	1.0	8.0	160
Th	Mα1	ThSiO ₄	PET	2.5	3.5	1700	0.5	5.0	600
U	Mα1	UO ₂	PET	2.6	2.5	1700	1.0	6.0	800
Pb	Mα1	PbS	PET	4.5	2.5	1700	1.0	5.0	200
La	Lαa1	LaPO ₄	LiF	2.0	2.0	1700	1.0	5.0	415
Ce	Lα1	CePO ₄	LiF	3.0	2.0	1700	1.0	5.0	350
Pr	Lβ1	PrPO ₄	LiF	1.5	1.5	1700	1.0	5.0	600
Nd	Lα1	NdPO ₄	LiF	2.0	2.5	1700	1.0	5.0	315
Sm	Lβ1	SmPO ₄	LiF	1.5	4.5	1700	1.0	5.0	550
Gd	Lβ1	GdPO ₄	LiF	1.2	1.0	1700	1.0	5.0	655
Dy	Lβ1	DyPO ₄	LiF	8.4	1.1	1700	1.0	5.0	670
Ho	Lβ1	HoPO ₄	LiF	3.3	7.0	1700	1.0	5.0	635
Er	Lα1	ErPO ₄	LiF	3.3	1.0	1700	1.0	5.0	400
Yb	Lα1	YbPO ₄	LiF	1.6	8.7	1700	1.0	5.0	400
Y	Lα1	YPO ₄	LiF	3.0	−3.0	1700	0.8	3.2	100

Negative value for background (Bkg) indicates that both background measurements were taken on the same side of the peak measurement to prevent major-element peak interferences. Detection limit for 12 000 nA s analyses (Tables 5 and 6).

Table 3: Correction factors for inter-element interference in EMP analyses (accelerating voltage 15 keV)

Analyzed line	Interfering line(s)	Correction factor*
P Kα1,2	Y Lβ1	0.0506
Pb Mα	Th M2-O4 + Th Mζ1	— †
	Th Mζ2	
Pb Mα	Y Lγ2,3	0.0075
U Mα2	Th Mβ	0.0128
Nd Lα1	Ce Lβ1,4	0.0027
Gd Lβ1	Ho Lα1	1.1540‡
Er Lα1	Tb Lβ1,4	0.0427§

*Correction factor = (measured wt % oxide of element x in x-free standard y)/(wt % oxide y in standard).

†No correction factor calculated; apparent PbO as a result of Th interference is below EMP detection limit at analytical conditions.

‡Correction calculated only for xenotime, as Ho concentration in monazite is generally at or near detection limit.

§Tb concentration estimated, not measured; 0.2 wt % Tb₂O₃(Mnz), 0.7 wt % Tb₂O₃(Xno).

Σ wt % oxide < 103 and 1.975 < sum cations < 2.025 are included for analysis and discussion ($n_{\text{Mnz}} = 526$, $n_{\text{Xno}} = 56$).

Pelitic xenotime is remarkably uniform in yttrium and heavy REE (HREE) contents (Table 4). Mole fraction YPO₄ ranges from 0.71 to 0.87, with an average value of 0.791 ± 0.025 . Dy, Yb, Gd, and Er are the other major constituents of xenotime, along with minor Ho; mole fraction HREEPO₄ ranges from 0.12 to 0.25, with an average value of 0.195 ± 0.021 . Xenotime light REE (LREE) content is low; Nd is present in all analyzed xenotime grains (0.05–1.02 wt % Nd₂O₃, average 0.30 ± 0.16 wt %); La, Ce, Pr, and Sm range from below detection limit to a few tenths of 1 wt %. Xenotime Th content is low, with a maximum Ca(Th,U,Pb)(PO₄)₂ (brabantite) component of 3.0 mol % and generally negative calculated (Th,U,Pb)SiO₄ (huttonite) component. Xenotime is slightly depleted in Pb with respect to coexisting monazite, with PbO content between <0.02 and 0.26 wt % (average 0.11 ± 0.05 wt %).

Monazite is, on average, 1–2 orders of magnitude more abundant than xenotime in the pelites studied. Representative monazite analyses from 25 samples are listed in Table 5. In contrast to xenotime, pelitic monazite is compositionally fairly variable. Monazite is largely a (La–Sm)PO₄ solid solution [(La–Sm)PO₄ = 0.75–0.97,

Table 4: Representative analyses of xenotime (values in wt % oxide)

Sample:	BF-55	BF-15	93-19	BF-17	BF-38	TM- 445	TM- 637	SP- 9B1	89-9	89-22	BF-78	BF-92	BF-14	V6B	V7D
Analysis:	525/2	204/2	187	178	179	455	415	18	464	261/3	65/1	577/2	129/1	7	6
P ₂ O ₅	34.09	34.97	35.96	36.82	35.56	36.37	35.71	36.38	35.87	36.53	36.67	35.34	35.62	37.78	36.72
SiO ₂	2.13	0.27	0.15	0.53	0.54	0.26	0.56	0.13	0.62	0.10	0.20	0.94	0.14	0.15	0.08
CaO	0.14	0.05	0.04	0.14	0.09	0.13	0.12	0.11	0.07	0.07	0.04	0.09	n.d.	0.07	0.03
PbO	0.11	n.d.	0.10	n.d.	n.d.	n.d.	0.17	0.03	0.17	n.d.	n.d.	0.10	n.d.	0.05	0.06
ThO ₂	0.78	0.42	0.35	n.d.	0.05	n.d.	n.d.	0.15	0.07	n.d.	n.d.	0.16	0.23	0.11	0.11
UO ₂	n.d.	0.08	n.d.	n.d.	0.25	0.69	1.72	n.d.	0.25	n.d.	n.d.	0.22	n.d.	n.d.	n.d.
Y ₂ O ₃	40.43	42.47	42.85	44.88	43.28	46.03	42.79	44.25	43.83	44.31	43.87	47.12	43.11	47.23	44.24
La ₂ O ₃	n.d.	n.d.	n.d.	n.d.	n.d.	n.d.	n.d.	n.d.	n.d.	0.05	n.d.	n.d.	n.d.	0.10	n.d.
Ce ₂ O ₃	n.d.	n.d.	n.d.	n.d.	n.d.	n.d.	0.32	n.d.	n.d.	0.05	n.d.	0.07	0.05	0.06	0.12
Pr ₂ O ₃	n.d.	0.18	n.d.	n.d.	n.d.	n.d.	n.d.	n.d.	0.07	n.d.	n.d.	n.d.	n.d.	n.d.	0.08
Nd ₂ O ₃	0.06	0.19	0.13	0.06	0.15	0.28	0.36	0.21	0.15	0.41	0.28	0.32	0.44	0.20	0.39
Sm ₂ O ₃	n.d.	n.d.	0.25	n.d.	n.d.	0.23	0.18	0.31	n.d.	n.d.	n.d.	n.d.	n.d.	n.d.	0.06
Gd ₂ O ₃	5.36	2.37	3.28	2.93	2.33	2.53	2.33	1.58	1.24	2.09	1.83	2.45	1.36	2.07	2.84
Dy ₂ O ₃	8.79	5.37	7.20	8.56	5.98	7.20	6.05	3.52	3.28	6.00	5.60	6.93	4.98	6.77	7.11
Ho ₂ O ₃	1.02	1.18	1.29	1.22	1.17	1.64	1.42	1.19	1.13	1.50	1.47	1.29	1.42	1.25	1.55
Er ₂ O ₃	3.46	4.80	4.60	2.54	4.25	3.10	4.15	4.75	5.52	4.54	4.88	3.23	5.72	2.63	3.96
Yb ₂ O ₃	2.46	4.66	3.65	1.28	4.04	0.93	3.15	6.75	6.81	3.83	4.91	1.41	6.07	2.02	2.43
Total	98.83	97.01	99.85	98.96	97.69	99.39	99.03	99.36	99.08	99.48	100.11	99.67	99.14	100.49	99.84
X _{PMO}	0.7504	0.7868	0.7740	0.8134	0.7964	0.8187	0.7831	0.7988	0.7980	0.7986	0.7938	0.8260	0.7812	0.8355	0.7965

n.d., element below detection limit.

Table 5: Representative analyses of monazite (values in wt % oxide)

Sample:	BF-55A	TM- 549	93-19	PUT92C2	PUT92 C2	BF-15	BF-15	BF-17	BF-17	BF-64	BF-52	BF-18	BF-57
	523/3	143	195/4	(A)	(B)	(A)	(B)	(A)	(B)	161/2	222/1	236/3	5/4
Analysis:				460	461	190/3	200/4	151/6	171/1				
P ₂ O ₅	28.46	25.72	29.75	29.47	30.12	28.83	29.75	29.33	29.25	29.76	29.70	29.65	29.71
SiO ₂	0.22	1.59	0.38	0.60	0.16	0.46	0.14	0.52	0.18	0.16	0.51	0.17	0.19
CaO	0.32	0.79	1.14	1.73	0.60	1.58	0.67	1.41	0.73	0.68	1.45	0.69	0.97
PbO	n.d.	n.d.	0.18	0.18	0.08	0.13	0.06	0.15	0.09	0.09	0.05	0.12	0.05
ThO ₂	1.84	4.41	6.52	9.48	2.94	9.70	3.56	8.54	3.92	4.12	9.13	4.01	5.08
UO ₂	n.d.	n.d.	0.26	0.51	0.08	0.41	n.d.	0.41	n.d.	n.d.	0.15	n.d.	0.19
Y ₂ O ₃	1.22	0.99	1.39	0.18	1.36	1.54	1.48	0.36	0.92	0.53	0.56	1.43	1.67
La ₂ O ₃	14.51	14.26	13.84	12.88	14.91	13.42	14.52	13.39	14.44	15.14	12.44	14.15	13.19
Ce ₂ O ₃	32.30	29.18	27.85	26.51	30.66	26.49	30.58	27.14	29.68	30.71	27.50	30.39	28.63
Pr ₂ O ₃	3.35	2.75	2.58	2.70	2.89	2.61	3.03	2.79	3.23	3.12	2.98	2.93	2.99
Nd ₂ O ₃	13.01	12.87	11.64	11.91	12.48	10.88	12.62	12.18	13.49	12.87	12.08	12.25	12.31
Sm ₂ O ₃	1.83	1.93	2.27	2.12	1.87	1.92	1.98	1.93	2.24	2.15	2.15	1.99	1.90
Gd ₂ O ₃	1.46	1.68	2.11	1.39	1.14	2.20	1.68	1.32	1.60	1.34	2.01	1.66	1.61
Dy ₂ O ₃	0.90	0.63	0.59	0.26	0.45	0.63	0.66	0.25	0.31	0.27	0.22	0.76	0.96
Ho ₂ O ₃	n.d.	0.08	n.d.	0.07	0.23	0.07	0.20	0.24	0.24	n.d.	n.d.	0.19	0.18
Er ₂ O ₃	0.06	0.19	n.d.	0.04	n.d.	0.12	0.04	0.06	0.05	n.d.	0.05	n.d.	0.08
Yb ₂ O ₃	n.d.	0.10	0.04	n.d.	n.d.	n.d.	0.09	n.d.	n.d.	0.15	n.d.	n.d.	n.d.
Total	99.48	97.17	100.54	100.03	99.97	100.99	101.06	100.02	100.37	100.94	100.98	100.39	99.71
X _{LiREE}	0.9149	0.8726	0.8265	0.8083	0.8954	0.7755	0.8770	0.8268	0.8878	0.9016	0.8149	0.8717	0.8412
X _{HREE}	0.0305	0.0343	0.0352	0.0229	0.0234	0.0381	0.0336	0.0242	0.0279	0.0222	0.0295	0.0336	0.0361
X _{Yut}	0.0029	0.0062	0.0145	0.0184	0.0025	0.0246	0.0042	0.0224	0.0053	0.0092	0.0222	0.0077	0.0069
X _{Yb}	0.0266	0.0663	0.0950	0.1466	0.0504	0.1304	0.0550	0.1190	0.0601	0.0560	0.1219	0.0575	0.0810
X _{YPO}	0.0251	0.0206	0.0289	0.0038	0.0283	0.0314	0.0302	0.0076	0.0189	0.0110	0.0116	0.0295	0.0348

Sample:	BF-58	TM-445	TM-637	TM-637	BF-38	SP-9B1	SP-9B1	89-22	89-22	89-9	89-9	BF-78	BF-78	BF-92
Analysis :	34/3	453	447/1	433/6	131/4	22	24	230/2	236/3	469/3	492/5	54/3	77/4	567/2
P ₂ O ₅	29.95	30.16	29.94	29.78	29.72	29.75	30.20	29.14	30.02	29.59	30.37	30.14	29.27	29.86
SiO ₂	0.23	0.15	0.15	0.10	0.57	0.34	0.16	0.51	0.09	0.09	0.15	0.09	0.10	0.07
CaO	0.70	0.94	0.90	0.74	0.98	1.31	0.69	1.50	0.91	0.68	0.93	0.94	0.97	0.87
PbO	0.09	0.07	0.05	0.09	0.08	n.d.	0.08	0.13	0.10	n.d.	0.21	0.24	0.16	n.d.
ThO ₂	3.73	4.31	4.58	2.66	4.22	6.67	3.06	8.63	3.25	3.03	3.81	3.97	4.37	3.97
UO ₂	n.d.	n.d.	0.35	0.49	0.30	0.59	0.09	0.40	0.53	n.d.	0.58	0.49	0.23	0.15
Y ₂ O ₃	1.55	1.69	1.68	2.02	1.85	2.09	2.07	0.35	2.36	1.66	2.51	2.77	0.61	2.32
La ₂ O ₃	14.15	13.66	13.94	14.57	14.00	12.83	13.89	12.91	14.25	15.14	13.97	13.47	14.44	13.82
Ce ₂ O ₃	30.03	28.77	29.29	28.64	29.36	26.22	28.71	27.66	28.92	29.98	28.36	28.58	30.68	30.26
Pr ₂ O ₃	3.05	2.88	3.19	2.88	2.93	2.70	2.85	2.93	2.84	2.98	2.97	2.86	3.00	2.74
Nd ₂ O ₃	12.74	12.30	12.24	11.89	12.32	11.12	12.33	13.38	12.86	12.20	11.85	12.01	12.46	11.71
Sm ₂ O ₃	2.15	1.88	2.35	2.28	1.96	2.14	2.05	2.17	1.80	1.98	2.05	1.36	2.11	1.67
Gd ₂ O ₃	1.37	1.68	1.98	1.97	1.53	1.63	1.84	1.41	1.81	1.36	2.12	1.74	1.52	1.47
Dy ₂ O ₃	0.36	0.69	0.39	0.78	0.81	0.88	0.96	0.12	0.94	0.57	0.73	0.91	0.52	0.54
Ho ₂ O ₃	n.d.	0.17	n.d.	0.15	n.d.	n.d.	0.31	n.d.	0.19	0.13	0.18	0.27	0.13	0.13
Er ₂ O ₃	n.d.	0.04	0.04	0.14	0.09	0.15	0.13	n.d.	0.15	0.07	0.15	n.d.	n.d.	0.08
Yb ₂ O ₃	n.d.	n.d.	0.06	0.06	n.d.	n.d.	n.d.	0.10	n.d.	0.14	0.09	n.d.	n.d.	n.d.
Total	100.10	99.31	101.13	99.24	100.72	98.42	99.42	101.34	101.27	99.60	101.03	99.84	100.57	99.66
X _{LiREE}	0.8823	0.8525	0.8538	0.8586	0.8506	0.7549	0.8212	0.8297	0.8430	0.8818	0.8289	0.8246	0.8785	0.8516
X _{HREE}	0.0222	0.0333	0.0314	0.0396	0.0306	0.0424	0.0521	0.0207	0.0385	0.0288	0.0410	0.0372	0.0275	0.0282
X _{Yut}	0.0051	−0.0001	0.0066	−0.0021	0.0001	0.0118	−0.0003	0.0184	−0.0033	−0.0014	0.0020	0.0029	0.0020	0.0003
X _{Yb}	0.0582	0.0790	0.0738	0.0619	0.0808	0.1367	0.0730	0.1241	0.0740	0.0564	0.0768	0.0781	0.0795	0.0721
X _{YPO}	0.0322	0.0353	0.0344	0.0419	0.0379	0.0542	0.0540	0.0071	0.0478	0.0344	0.0513	0.0572	0.0125	0.0478

Table 5: continued

Sample:	BF-92 (B)	BF-14P (A)	BF-14P (B)	LM1A2 (A)	LM1A2 (B)	LM1A2 (C)	V6A (A)	V6A (B)	V6B (A)	V6B (B)	V7C (A)	V7C (B)	V7D (A)	V7D (B)
Analysis:	572/1	104/7	138/6	164/1	166/3	178/3	290/5	292/1	8	13	297/2	305/2	3	4
P ₂ O ₅	30.11	29.72	28.43	29.07	29.74	29.78	30.61	30.96	30.40	30.49	29.54	31.30	30.57	29.96
SiO ₂	0.05	0.12	0.21	0.08	0.10	0.07	0.18	0.12	0.07	0.29	0.50	0.31	0.20	0.18
CaO	0.84	1.00	0.89	1.64	0.94	1.02	1.06	1.32	0.63	1.02	1.60	0.96	0.83	0.89
PbO	n.d.	0.08	0.22	0.18	0.16	0.16	0.08	0.45	n.d.	n.d.	n.d.	0.10	n.d.	n.d.
ThO ₂	3.99	4.59	4.33	8.32	4.84	4.56	5.58	5.40	1.98	5.30	8.85	5.03	3.47	4.32
UO ₂	0.27	0.58	n.d.	0.27	n.d.	0.24	0.18	0.33	0.33	0.25	0.25	n.d.	n.d.	0.14
Y ₂ O ₃	0.82	3.16	0.76	1.20	0.30	2.90	0.20	2.79	4.91	0.19	0.36	3.25	2.62	1.01
La ₂ O ₃	14.01	12.75	14.24	12.58	14.26	13.04	15.13	13.28	11.94	15.17	13.73	13.61	14.84	14.34
Ce ₂ O ₃	32.01	27.35	30.28	27.05	30.48	28.11	31.50	28.20	25.70	30.44	28.97	28.74	28.63	29.25
Pr ₂ O ₃	2.71	2.89	3.15	2.89	2.87	2.68	2.83	2.75	2.83	2.84	2.81	2.63	2.69	3.03
Nd ₂ O ₃	11.84	12.48	13.08	12.67	13.53	12.21	11.46	11.19	10.98	11.70	11.18	11.07	10.59	11.71
Sm ₂ O ₃	1.61	2.21	1.95	2.28	2.05	1.86	1.29	1.33	1.67	1.49	1.65	1.57	1.38	1.86
Gd ₂ O ₃	1.41	1.99	1.48	1.74	1.56	1.93	0.96	1.48	3.36	0.59	0.95	1.54	1.40	1.35
Dy ₂ O ₃	0.21	0.95	0.32	0.59	0.19	0.83	0.27	1.05	1.84	n.d.	0.16	1.08	0.52	0.40
Ho ₂ O ₃	0.08	0.28	n.d.	0.06	0.06	n.d.	n.d.	0.25	0.08	n.d.	n.d.	0.15	0.16	0.15
Er ₂ O ₃	n.d.	0.21	0.06	0.14	n.d.	0.14	n.d.	0.08	0.17	n.d.	n.d.	0.20	0.16	0.06
Yb ₂ O ₃	n.d.	0.11	0.11	0.05	0.06	n.d.	n.d.	n.d.	0.17	n.d.	n.d.	0.07	0.06	0.07
Total	99.96	100.47	99.51	100.81	101.14	99.53	101.33	100.98	97.06	99.77	100.55	101.61	98.12	98.72
X _{REE}	0.8879	0.8045	0.8817	0.7996	0.8875	0.8169	0.8839	0.7975	0.7744	0.8947	0.8300	0.8103	0.8475	0.8739
X _{HREE}	0.0220	0.0443	0.0255	0.0322	0.0236	0.0370	0.0157	0.0361	0.0734	0.0078	0.0150	0.0381	0.0300	0.0265
X _{lut}	0.0027	0.0047	0.0034	0.0092	0.0054	0.0015	0.0074	0.0003	−0.0059	0.0068	0.0139	0.0054	−0.0039	0.0026
X _{nb}	0.0704	0.0821	0.0739	0.1346	0.0773	0.0849	0.0888	0.1090	0.0536	0.0868	0.1336	0.0795	0.0708	0.0756
X _{po}	0.0170	0.0644	0.0155	0.0244	0.0062	0.0597	0.0042	0.0571	0.1045	0.0039	0.0075	0.0667	0.0556	0.0214

n.d., element below detection limit.

Table 6: Representative trace-element analyses of major pelitic phases (concentrations in ppm)

Sample grade: Sample:	garnet 93-19A biotite	garnet BF-15B garnet ¹	staurolite BF-38 biotite	staurolite BF-38 staurolite	staurolite BF-64 garnet ²	sillimanite BF-78 biotite	sillimanite BF-78 muscovite	sillimanite BF-78 sillimanite
Y	0.2	2076 (76)	1	<0.2	2678 (59)	<0.2	<0.3	3
La	<0.3	<0.5	n.a.	n.a.	<2	<0.2	<0.5	<3
Ce	1	<0.2	0.8	<0.1	<1	<0.1	<0.18	<2
Pr	n.a.	<0.3	n.a.	n.a.	<1	n.a.	n.a.	n.a.
Nd	<0.7	<0.7	<0.7	<0.5	<3	<0.5	<0.7	<6
Sm	<2	2	<1.7	<0.9	3 (0.5)	<0.9	<3	<16
Eu	<0.3	1.4 (0.0)	<0.3	<0.2	0.9 (0.02)	<0.3	0.6	<4
Gd	<2	19 (0.4)	<1.3	<1	57 (7.1)	<1	<2	<13
Tb	n.a.	13 (0.4)	n.a.	n.a.	29 (2.8)	n.a.	n.a.	n.a.
Dy	n.a.	225 (0.0)	<0.4	<0.2	333 (7.1)	n.a.	n.a.	n.a.
Ho	n.a.	98 (4.9)	n.a.	n.a.	102 (4.2)	n.a.	n.a.	n.a.
Er	n.a.	465 (60.1)	<0.3	<0.2	338 (56.6)	n.a.	n.a.	n.a.
Tm	n.a.	17 (37)	n.a.	n.a.	55 (16.3)	n.a.	n.a.	n.a.
Yb	n.a.	998 (352.8)	<0.2	<0.2	396 (167.6)	n.a.	n.a.	n.a.
Lu	n.a.	154 (62.9)	<0.1	<0.1	56 (27.6)	n.a.	n.a.	n.a.
Pb	n.a.	<0.3	n.a.	n.a.	<1	n.a.	n.a.	n.a.
Th	0.3	<0.1	0.4	<0.1	<0.3	<0.1	<0.1	<1
Y (NIST-610)	466 (5.2)	450 (3.8)	466 (5.8)	466 (5.8)	450 (12.3)	466 (5.5)	466 (5.5)	466 (5.5)

Table 6: continued

Sample grade: Sample:	sillimanite 89-22B plagioclase ³	sillimanite 89-22B garnet ⁴	migmatite BF-14P biotite	migmatite BF-14P muscovite	migmatite BF-14P garnet ⁵ (A)	migmatite BF-14P garnet ⁶ (B)	migmatite V7D (4) plagioclase ⁷	migmatite V7D garnet ⁸
Y	<4	245 (9.9)	<0.3	<0.4	1098 (5.6)	232 (27.6)	<6	228 (17.7)
La	5	<0.9	<0.2	<0.4	n.a.	n.a.	18 (1.5)	<0.7
Ce	8	<0.5	<0.1	<0.2	n.a.	n.a.	26 (1.4)	<0.2
Pr	<1	<0.5	n.a.	n.a.	n.a.	n.a.	2 (0.3)	<0.4
Nd	4	<2	<0.7	<0.6	n.a.	n.a.	8 (0.9)	<1
Sm	<4	<3	<1	<2	3 (0.2)	0.3 (1.7)	<4	3 (2.0)
Eu	<1	<0.7	<0.3	1	0.1 (0.02)	1 (0.5)	6 (0.5)	<0.4
Gd	<3	<2	<1	<2	16 (0.7)	5 (0.7)	<4	16 (3.9)
Tb	<0.5	2 (0.1)	n.a.	n.a.	n.a.	n.a.	<0.5	6 (0.6)
Dy	<2	27 (1.3)	n.a.	n.a.	122 (0.7)	34 (2.8)	<1	44 (1.6)
Ho	<0.8	10 (0.2)	n.a.	n.a.	n.a.	n.a.	<0.8	9 (0.07)
Er	<0.9	35 (1.2)	n.a.	n.a.	175 (0.8)	29 (5.6)	<2	21 (0.7)
Tm	<0.3	6 (0.6)	n.a.	n.a.	n.a.	n.a.	<0.3	3 (0.4)
Yb	<0.9	49 (11)	n.a.	n.a.	273 (0.8)	29 (4.9)	<0.7	15 (3.6)
Lu	<0.3	6 (1.8)	n.a.	n.a.	43 (0.7)	4 (0.0)	<0.3	2 (0.8)
Pb	5	<0.7	n.a.	n.a.	n.a.	n.a.	25 (1.2)	<0.4
Th	1.5	<0.2	<0.1	<0.1	<0.1	<0.1	<0.1	<0.1
Y (NIST-610)	450 (2.5)	450 (5.2) ^{ed}	466 (5.5)	466 (5.5)	444 (11.5)	444 (11.5)	450 (10.8)	450 (3.8)

NIST-610 glass: average and standard deviation of four analyses, yttrium values reported.

¹Two analyses; core and rim of same garnet. Standard deviation on two analyses, core analysis reported.

²Two garnet cores analyzed. Standard deviation on two analyses, analysis 1 reported.

³One analysis.

⁴Two garnet cores analyzed. Standard deviation on two analyses, analysis 1 reported.

⁵Two analyses of 'anatectic region' of same garnet, average of both values reported.

⁶Two analyses of rim of same garnet (also same garnet as 5), average of both values reported.

⁷Analyses of four separate plagioclase cores; analysis 3 reported, standard deviation from all four analyses.

⁸Two garnet cores analyzed. Standard deviation on two analyses, analysis 1 reported.

n.a., not analyzed.

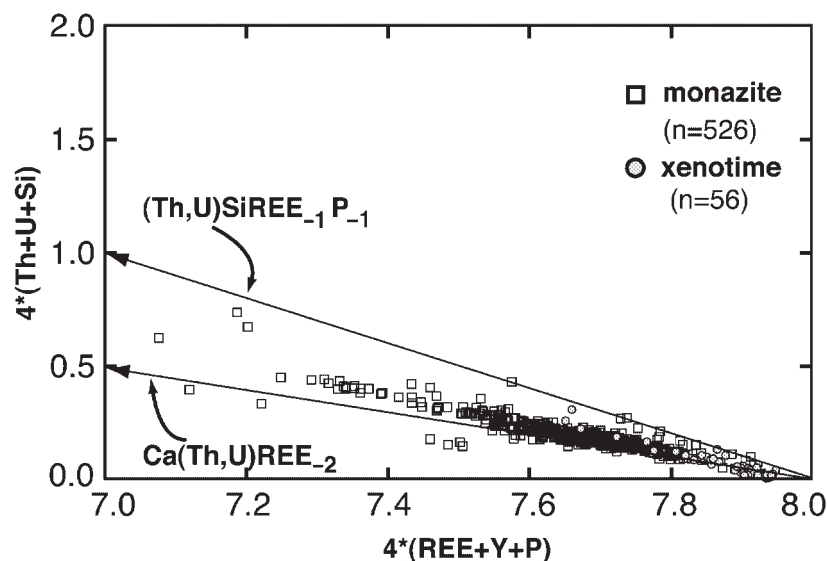


Fig. 1. Monazite and xenotime cation plot, normalized to 16 oxygens. REEPO_4 phosphate plots at (8,0) and brabantite $[\text{Ca}(\text{Th,U})\text{REE}_{-2}]$ and huttonite $[(\text{Th,U})\text{SiREE}_{-1}\text{P}_{-1}]$ exchange vectors are plotted. Huttonite exchange in monazite is analogous to zircon ($\text{ZrSiREE}_{-1}\text{P}_{-1}$) exchange in xenotime.

average 0.860 ± 0.030], but displays considerable variation in mole fraction of $(\text{Y} + \text{HREE})\text{PO}_4$ (0.01–0.18) and brabantite mole fraction (0.00–0.17). Huttonite component is generally close to zero or negative. Measured monazite PbO content ranges from <0.02 to 0.45 wt % (average 0.12 ± 0.08 wt %). Formulae for calculation of REE phosphate components are given in the Appendix. The grouping of Pb with Th and U in both the huttonite and brabantite components, rather than with Ca in the brabantite component, is based on the interpretation that all lead in both monazite and xenotime is derived by radioactive decay of a portion of the Th and U present at the time of monazite crystallization (Parrish, 1990). Measured PbO content in both phases is in general agreement with PbO content calculated using associated Th and U values and assuming an average age of 350 Ma.

The extent of brabantite vs huttonite exchange operational in monazite and xenotime is depicted in a plot of $\text{Th} + \text{U} + \text{Si}$ vs $\text{REE} + \text{Y} + \text{P}$ (Fig. 1). The brabantite exchange vector is clearly dominant in monazite. Owing to low concentrations of Ca, Th, U, and Si in monazite, the relative contributions of brabantite and huttonite exchange in xenotime are obscured. However, it is noted that the huttonite exchange in monazite is equivalent to the zircon exchange ($\text{ZrSiREE}_{-1}\text{P}_{-1}$) in xenotime.

The decay of Th and U (+4) to Pb creates a charge imbalance in monazite, as it is generally accepted that, under most conditions of T and $f\text{O}_2$ corresponding to regional metamorphism, +2 is the stable oxidation state

of lead (Watson *et al.*, 1997, and references therein). However, this charge imbalance is slight, because of low monazite Pb content. Overall, examination of all monazite analyses suggests that monazites in these samples are very nearly charge balanced. The means and standard deviations of the cation sums (calculated on an 8 oxygen basis) are as follows: $\text{Si} + \text{P} = 0.997 \pm 0.020$; $\text{REE} + \text{Y} + \text{Th} + \text{U} + \text{Pb} + \text{Ca} = 1.007 \pm 0.032$; $\text{Ca} - (\text{Th} + \text{U} + \text{Pb}) = -0.005 \pm 0.006$; $\text{Ca} + \text{Si} - (\text{Th} + \text{U} + \text{Pb}) = 0.005 \pm 0.018$. Figure 2 shows frequency histograms for $\text{Si} + \text{P}$ and $\text{Ca} + \text{Si} - (\text{Th} + \text{U} + \text{Pb})$ in monazite. Both frequency distributions are approximately normal; high outliers in the $\text{Ca} + \text{Si} - (\text{Th} + \text{U} + \text{Pb})$ plot are from high-Si, low-Th monazite analyses that probably result from subsurface micro-inclusions of quartz in monazite. The slightly positive value of $\text{Ca} + \text{Si} - (\text{Th} + \text{U} + \text{Pb})$ suggests that there may be a slight Si excess in the analyzed monazites. To help rule out the possibility of systematic analytical error, $\text{Si} + \text{P}$ and $\text{Ca} + \text{Si} - (\text{Th} + \text{U} + \text{Pb})$ were calculated for 46 monazite analyses taken from Franz *et al.* (1996), Finger *et al.* (1998), Förster (1998), and Zhu & O’Nions (1999a). Values from those studies are nearly identical to our data (Fig. 2c and d), and the mean $\text{Si} + \text{Ca} - (\text{Th} + \text{U} + \text{Pb})$ parameter is slightly positive (0.005).

Importantly, examination of Table 5 reveals that much of the compositional variation in monazite is intragranular. Variations of up to ± 8.5 wt % ThO_2 (sample PUT-92C2) and ± 4.5 wt % Y_2O_3 (sample V6B) have been recorded within a single grain of monazite.

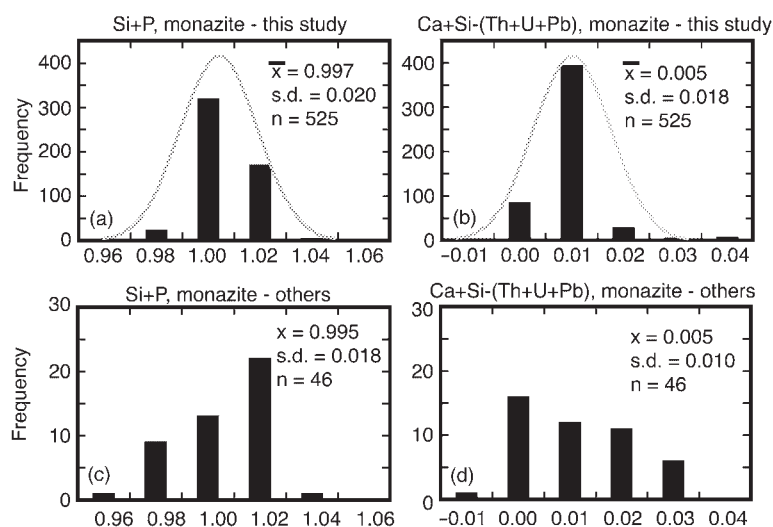


Fig. 2. Monazite cation sum frequency distribution histograms for this dataset (a, b) and for monazite analyses from Franz *et al.* (1996), Finger *et al.* (1998), Förster (1998), Zhu & O'Nions (1999a) (c, d). Cation sums plotted are Si + P (a, c) and Ca + Si – (Th + U + Pb) (b, d). The mean and standard deviation of each sum is listed on each plot, along with the number of sums in each distribution. The distribution of cation sums in these datasets approximates a gaussian (normal) distribution [gray curves in (a) and (b)], and there is an average excess of Ca + Si over Th + U + Pb in each dataset, suggesting substitution of some Si for P in (REE,Y)PO₄, with resultant charge deficit.

The implications of monazite intragranular compositional variation are addressed below.

Apatite compositions

Analyses from this suite of samples indicate apatite Σ LREE (La–Sm) contents of the order of ~ 500 – 1000 ppm, and $X_{\text{OH-apatite}}$ of the order of 0.01 – 0.40 . These REE numbers are lower than those of apatites from disparate diagenetic and metamorphic environments. For example, apatite from a clay-rich aquitard (Yan *et al.*, 2000) contains Σ LREE ~ 3800 ppm, apatite from migmatite (Bea, 1996) contains Σ LREE ~ 4750 ppm. Cruft (1966) found that apatites from marble and pyroxenite contain 2000 – $22\,000$ ppm Y + La + Ce. Finger *et al.* (1998) found Σ LREE content of $\geq 15\,000$ ppm in apatite coronas around monazite in amphibolite-facies gneiss. Apatite may therefore be a significant contributor to the overall REE budget of a metamorphic rock, but the low abundance of REE in apatite in this suite of samples would require apatite mass of approximately three orders of magnitude greater than that of monazite to equal the contribution of monazite to the REE budget.

Of particular interest is the wide variation in OH-Ap component in apatite (0.0 – 0.40). In general, apatite included in garnet cores contains a larger fraction of the hydroxy-component than matrix apatite grains. Apatite Cl-component is near zero except for apatite grains from migmatitic sample V7C (Spear & Parrish, 1996); analyzed apatites (six grains, 10 spots) contain 0.11 – 0.13 $X_{\text{Cl-Ap}}$.

Major phase trace-element compositions

LA-ICP-MS analyses of several major pelite phases (Table 6) show the following.

(1) Biotite, muscovite, staurolite, and sillimanite (along with quartz) constitute the majority of the mineral mode (≥ 80 vol. %) and all contain negligible concentrations of REE, Y, Th, U, and Pb. These numbers are similar to the concentrations of REE, Y, Th, U, and Pb in biotite and muscovite reported by Bea (1996) and Yang & Rivers (2000), both of whom noted that high REE contents in earlier analyses of micas (Bea *et al.*, 1994; Yang *et al.*, 1999) were probably due to minute inclusions of monazite, apatite, or xenotime.

(2) Plagioclase contributes a small, but non-negligible, amount of LREE to the whole-rock budget; sillimanite-zone plagioclase contains 17 ppm (La + Ce + Nd) and the LREE content of plagioclase increases to 52 ppm (La + Ce + Nd) in plagioclase from migmatite zone samples. Plagioclase from high-grade samples studied by Bea (1996) and Kretz *et al.* (1999) contain similar (La + Ce + Nd).

(3) Garnet is a significant major-phase host for HREE (Table 6), with HREE (Gd–Lu) content ≥ 2000 ppm in xenotime-bearing garnet-zone samples; X_{HREE} in garnet decreases with increasing metamorphic grade, analogous to the observed decrease of YAG component in garnet with increasing metamorphic grade (Pyle & Spear, 2000a). (YAG: $\text{Y}_3\text{Al}_2\text{Al}_3\text{O}_{12}$). HREE content of garnet in xenotime-absent samples is lower than the HREE content of garnet in xenotime-bearing samples of the same metamorphic grade.

Assessment of equilibrium between monazite and xenotime

The complexity of monazite intragrain compositional variation hinted at by spot analyses (Table 5) is revealed in monazite element distribution maps (Fig. 3). Approximately 100 separate monazite grains were mapped for element distribution in the 28 samples studied; three examples from different metamorphic grades are shown in Fig. 3. Thorough study of monazite element distribution maps, spot analysis variation, and texture reveals the following:

(1) in a large number of grains, variation in back-scattered electron (BSE) intensity is due largely to changes in yttrium concentration (Fig. 3g–i), although, in other cases, Th concentration variation contributes significantly (Fig. 3d–f), or is responsible for all of the BSE contrast (Fig. 3a–c). The large role of Y variation in BSE intensity variation differs from that reported in other monazite-bearing suites (Watt & Harley, 1993; Watt, 1995).

(2) Discontinuous thorium zoning is more common in monazite from low-grade samples (Fig. 3a–c), although exceptions do occur (Fig. 3d–f).

(3) If monazite is strongly zoned in thorium, the form of zoning generally consists of a Th-rich core and Th-poor outer region (Fig. 3c and f), whereas yttrium zonation may be bimodal, oscillatory, ‘patchy’, or a combination of the above forms (Fig. 3e and h).

(4) In garnet zone samples containing matrix xenotime, monazite yttrium distribution is largely homogeneous (Fig. 3b).

(5) Yttrium and thorium zoning may both vary strongly in an antithetic fashion (Fig. 3e and f), or still vary antithetically, but with much greater absolute yttrium variation than thorium variation (Fig. 3g–i).

(6) Monazites that are texturally associated with xenotime always have among the highest yttrium content of all monazites in that sample.

The non-correspondence of Th and Y zoning in monazite is an indication that different reservoirs are reacting to control monazite Y and Th distribution. Garnet growth has a profound effect on bulk-rock yttrium content and xenotime stability (Pyle & Spear, 1999, 2000a), and it follows that reaction of garnet exerts similar influence over the (Y,HREE) content of monazite. Factors controlling monazite Th distribution are less clear, as no other significant Th sink has been identified in these samples. Zircon of typical Th content (Bea, 1996) will exert some control over monazite Th distribution if the zircon is present in sufficient abundance and is not kinetically inhibited from reacting.

Criteria for inferring monazite–xenotime equilibrium

With the above observations as a guide, a set of criteria (Table 7) were established to aid in the interpretation

of stable coexistence of monazite and xenotime. The reference to inclusion of monazite and/or xenotime in *garnet* porphyroblasts is specific, as other porphyroblasts (specifically biotite and staurolite) do not contain (or display) noticeable yttrium zoning discontinuities. The existence of such Y discontinuities in garnet in this dataset is interpreted to mark the loss of xenotime from the mineral assemblage (Pyle & Spear, 1999), and, consequently, the discontinuation of monazite–xenotime equilibrium.

Using the Table 7 criteria as a guide, all monazite spot analyses were classified as having grown in either a xenotime-bearing or xenotime-absent mineral assemblage. The extent of compositional equilibration in monazite + xenotime assemblages is assessed by first examining the variation of Y, Dy, and Gd in all monazites (Fig. 4), followed by examination of monazite–xenotime Y/Gd and Y/Dy partitioning.

Compositional variation of monazite

The mole fraction of GdPO_4 component in monazite is largely insensitive to metamorphic grade (Fig. 4a–e), or the presence of xenotime in the mineral assemblage, and the value of $\text{GdPO}_4(\text{Mnz})$ clusters about 0.02. $\text{DyPO}_4(\text{Mnz})$ is uniformly low in xenotime-absent assemblages (≤ 0.01), but in xenotime-bearing assemblages correlates positively with $\text{YPO}_4(\text{Mnz})$, increasing to a maximum of ~ 0.015 in the migmatite zone (Fig. 4f–j). $\text{YPO}_4(\text{Mnz})$ in xenotime-bearing assemblages increases systematically with rising T , with maximum $\text{YPO}_4(\text{Mnz}) \sim 0.03$ for garnet zone monazite, ~ 0.05 for staurolite zone samples, ~ 0.06 for sillimanite zone samples, and ~ 0.08 for migmatite zone samples. The spread in $\text{YPO}_4(\text{Mnz})$ for high-grade xenotime-bearing samples results from either: (1) continuous monazite growth from garnet zone through to the maximum metamorphic grade, with xenotime as part of the assemblage at various points in the monazite growth history; or (2) multiple, separate episodes of monazite growth between garnet zone and migmatite zone P – T conditions, with xenotime present in the assemblage for each monazite growth episode. In either case, the large spread in $\text{YPO}_4(\text{Mnz})$ implies that monazite growth (whether continuous or discontinuous) in these samples occurred over a large part of the prograde P – T path.

Monazite grains in contact with, or in close textural proximity to, xenotime are shown with coexisting xenotime in ternary LREE–HREE–Y (Fig. 5a) and LREE–(HREE + Y)–Th plots (Fig. 5b). Figure 5a again shows the systematic increase in $\text{YPO}_4(\text{Mnz})$ with increasing metamorphic grade, but in addition shows that the increase of total Y + HREE(Mnz) occurs at a nearly constant Y/HREE ratio ($\sim 1:1$), regardless of xenotime

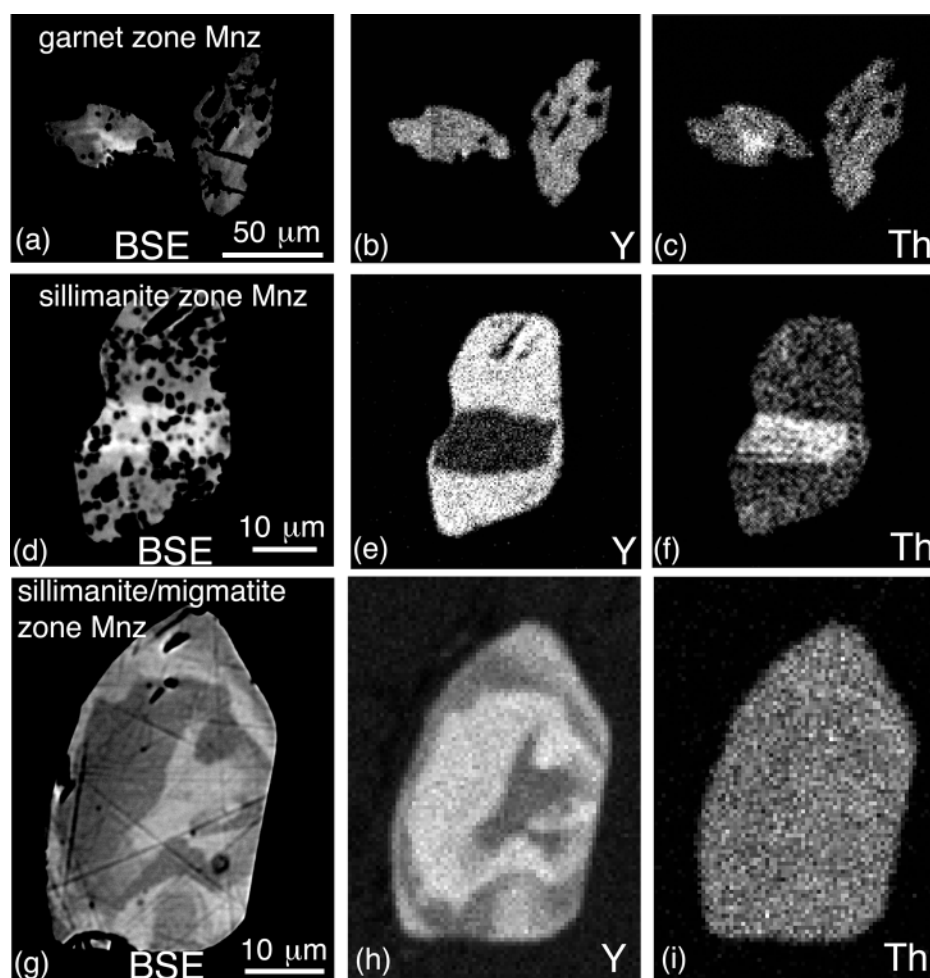
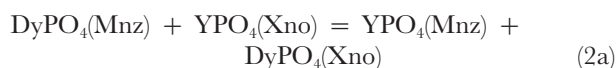
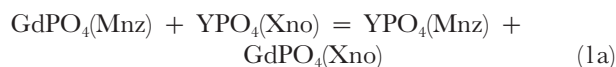


Fig. 3. Monazite back-scatter electron images, Y, and Th element distribution maps. Brighter areas indicate higher concentration of element. (a–c) Monazite, sample 93-19A (garnet zone). Y is roughly homogeneous, and Th decreases towards the monazite rim, corresponding to back-scatter zoning. (d–f) Monazite, sample 89-22 (sillimanite zone). Back-scatter brightness corresponds to Th enrichment, and Y zoning is antithetic to Th zoning. (g–i) Monazite, sample BF-78 (transitional sillimanite–migmatite zone). Th is nearly homogeneous, but Y is complexly zoned (corresponding to back-scatter variation), with at least four distinct compositional zones visible in the map.

composition; further evidence for temperature rather than bulk-composition control of monazite composition. The apparent tie-line crossovers evident in Fig. 5a are reduced by inclusion of total Th component as a plotting element (Fig. 5b). Total Th component of monazite coexisting with xenotime does not appear to be a strong function of temperature.

Monazite–xenotime element partitioning

Figure 6 is a plot of $\ln(YPO_4/i)(Mnz)$ vs $\ln(YPO_4/i)(Xno)$ for xenotime-bearing assemblages, as a function of metamorphic grade, where i is $GdPO_4$ (Fig. 6a–e), and $DyPO_4$ (Fig. 6f–j), and diagonal lines are isopleths of K_D for the reactions



with distribution coefficients

$$K_{D1} = \frac{\left(\frac{X_{YPO_4}}{X_{GdPO_4}} \right)_{Mnz}}{\left(\frac{X_{YPO_4}}{X_{GdPO_4}} \right)_{Xno}} \quad (1b)$$

Table 7: Ranked textural and compositional criteria for assumption of monazite–xenotime compositional equilibrium

Observed textural and/or compositional criteria	Assumption	Relative rank
Physical contact of monazite and xenotime grains	Both grains in (compositional) equilibrium	1
Y-homogeneous monazite and xenotime coexist in sample matrix (not necessarily in contact)	All matrix monazite and xenotime in equilibrium	2
Y-homogeneous monazite and xenotime included in same garnet, with no garnet yttrium discontinuities between the two inclusions	Included monazite and xenotime in equilibrium	3
Discontinuously Y-zoned monazite and xenotime coexist in sample matrix (not necessarily in contact)	Only high-Y portion of monazite in equilibrium with xenotime	4
Discontinuously Y-zoned monazite and xenotime included in same garnet, with no garnet yttrium discontinuities between the two inclusions	Only high-Y portion of monazite in equilibrium with xenotime	5
Discontinuously Y-zoned monazite included in specific garnet, and xenotime included in different grain of garnet, and both inclusions present in same type of ‘compositional domain’ within garnets	Only high-Y portion of monazite in equilibrium with xenotime	6
Discontinuously Y-zoned monazite included in garnet, and xenotime present in matrix	Only high-Y portion of monazite in equilibrium with xenotime	7
Monazite and some portion of occluding garnet are approximately homogeneous in Y, and monazite Y content is comparable to that of monazite in xenotime-bearing samples of the same metamorphic grade	Monazite grew with xenotime present in the mineral assemblage (now absent?)	8

$$K_{D2} = \frac{\left(\frac{X_{YPO_4}}{X_{DyPO_4}} \right)_{Mnz}}{\left(\frac{X_{YPO_4}}{X_{DyPO_4}} \right)_{Xno}}. \quad (2b)$$

Although care has been taken to plot only monazite grains that grew in a xenotime-bearing assemblage, it is unlikely that all monazite compositions in a single sample are in equilibrium with a single xenotime composition, as the latter shows some compositional variation. Therefore, between one and four $\ln(YPO_4/i)(Xno)$ values are plotted against the entire range of xenotime-equilibrated $\ln(YPO_4/i)(Mnz)$ values in an attempt to encompass the total compositional variability of xenotime in a given sample. For some samples, the range of xenotime compositions lies within the calculated analytical uncertainty. For others, xenotime displays a greater range in $\ln(YPO_4/GdPO_4)$ and $\ln(YPO_4/DyPO_4)$ than may be explained by analytical precision. Such compositional variability may be due to: (1) fractionation of non-essential xenotime components (e.g. Gd, Dy, Ho, Er, Yb) by garnet during or between periods of xenotime growth; (2) disequilibrium; or (3) P – T control over monazite–xenotime

element partitioning. Heinrich *et al.* (1997) showed that, whereas xenotime LREE content appears to increase with rising temperature, Dy and Gd content of xenotime appears to be independent of metamorphic grade. Differences in effective bulk composition as a result of fractionation of HREE by growing garnet should be reflected in a systematic difference in $\ln(YPO_4/GdPO_4)(Mnz)$, and $\ln(YPO_4/DyPO_4)(Mnz)$ as well, but such a sympathetic variation is not observed. The variation in $\ln(YPO_4/GdPO_4)$ and $\ln(YPO_4/DyPO_4)$ above and beyond that predicted by propagation of analytical uncertainty may reflect the ‘geological’ uncertainty associated with selecting equilibrium monazite–xenotime pairs when both minerals are zoned.

K_{D1} values for all samples cluster around a value of 0.05 (Fig. 6f–j), and K_{D2} values cluster around 0.3 (Fig. 6f–j). Intragrade variation of both distribution coefficients is greater than the variation in K_D between grades, with K_D values from migmatite-zone pairs displaying the greatest variation. This variation may reflect the more complex monazite reaction history of the highest-grade samples. In general, K_{D1} values show less overall variation than values of K_{D2} . This observation is borne out in a plot of average K_D vs metamorphic grade (Fig. 7). K_{D1} is

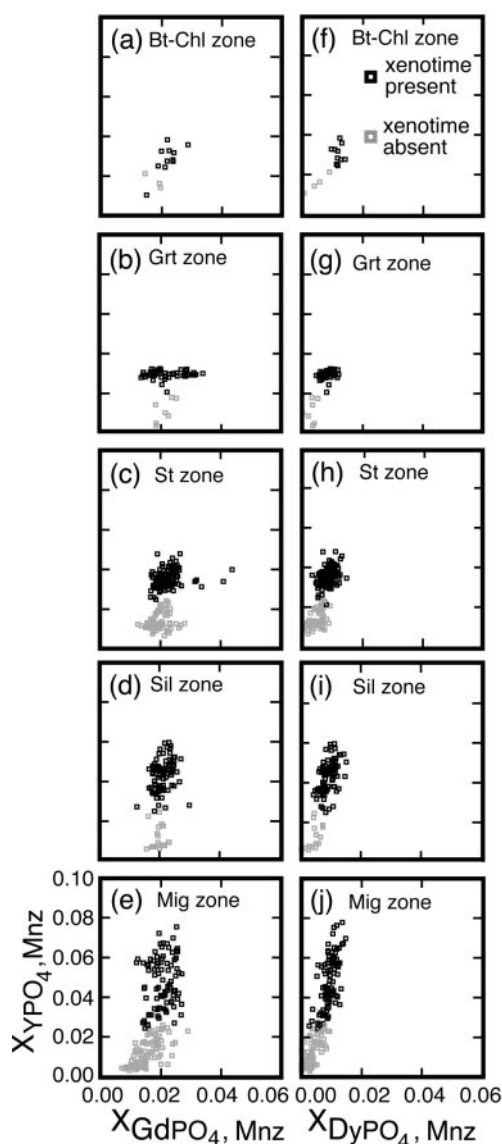


Fig. 4. Monazite composition plots. (a–e) $\text{YPO}_4(\text{Mnz})$ vs $\text{GdPO}_4(\text{Mnz})$ and (f–j) $\text{YPO}_4(\text{Mnz})$ vs $\text{DyPO}_4(\text{Mnz})$ for (a, f) biotite–chlorite zone samples, (b, g) garnet zone samples, (c, h) staurolite zone samples, (d, i) sillimanite zone samples, and (e, j) migmatite zone samples. Gray squares, monazite from xenotime-absent assemblages; black squares, monazite in equilibrium with xenotime. Interpretation of monazite–xenotime equilibrium based on criteria given in Table 7.

largely invariant with metamorphic grade (Fig. 7a), and $K_{\text{D}2}$ may correlate positively with temperature (Fig. 7b), but this variation may be obscured by uncertainties associated with analysis of Dy in monazite.

Application to monazite–xenotime thermometry

Coexisting monazite and xenotime in our sample suite have been shown to approach compositional equilibrium, based on the systematic behavior of monazite composition

(increasing X_{YPO_4} , constant Y/HREE) and monazite–xenotime element partitioning (nearly constant Y/Gd and Y/Dy). These findings are in accord with studies of synthetic (Gratz & Heinrich, 1997, 1998; Andrehs & Heinrich, 1998) and naturally occurring (Heinrich *et al.*, 1997) monazite–xenotime pairs. Furthermore, the monazite limb of the monazite–xenotime miscibility gap from this study (Fig. 8) is in excellent agreement with that of Heinrich *et al.* (1997), further evidence that these phases crystallized in near equilibrium.

Single-grain monazite ages (Parrish, 1990) and compositional maps clearly indicate that monazite growth is episodic and that determination of xenotime–monazite coexistence in samples with multi-stage monazite is non-trivial. Propagated temperature uncertainty associated with the monazite limb of the miscibility gap from this study is approximately $\pm 20^\circ\text{C}$, but application of a ‘monazite-limb’ thermometer to monazite that grew in a xenotime-absent assemblage can result in a temperature error of well over 100°C . For example, reaction history analysis of the monazite shown in Fig. 3 indicates that the outermost low-Y zone grew at sillimanite-zone temperature conditions (580 – 620°C) in a xenotime-absent mineral assemblage. Application of the Gratz & Heinrich (1997, 1998) thermometer to the outer low-Y portion of the monazite ($X_{\text{Y} + \text{HREE}} = 0.0418$) yields a temperature estimate of 392°C . In this situation, the source of most of the inaccuracy is ‘geological uncertainty’ (Kohn & Spear, 1991), rather than inaccuracy in thermometer calibration.

Assessment of equilibrium between monazite and garnet

The distribution of yttrium in garnet is a strong function of accessory phase assemblage, and, hence, effective (matrix) bulk composition. Garnet in xenotime-bearing samples undergoes a systematic decrease in YAG component with rising temperature (Pyle & Spear, 2000a), but loss of xenotime from the mineral assemblage results in rapid, Rayleigh-type fractionation of available Y into growing garnet (Pyle & Spear, 1999). HREEs in garnet behave identically to Y in both cases. LA-ICP-MS analyses (Fig. 9) demonstrate the systematic decrease of Yb and Er in garnet from xenotime-bearing samples with increasing metamorphic grade, parallel to the garnet yttrium trend.

The Y content of monazite depends strongly on whether xenotime is present. In xenotime-bearing assemblages, $a_{\text{YPO}_4}(\text{Mnz})$ is buffered by the presence of xenotime, and its value increases with rising temperature. In contrast, in xenotime-absent assemblages, garnet and monazite may continue to grow and the remaining Y and HREE will be depleted as they are incorporated

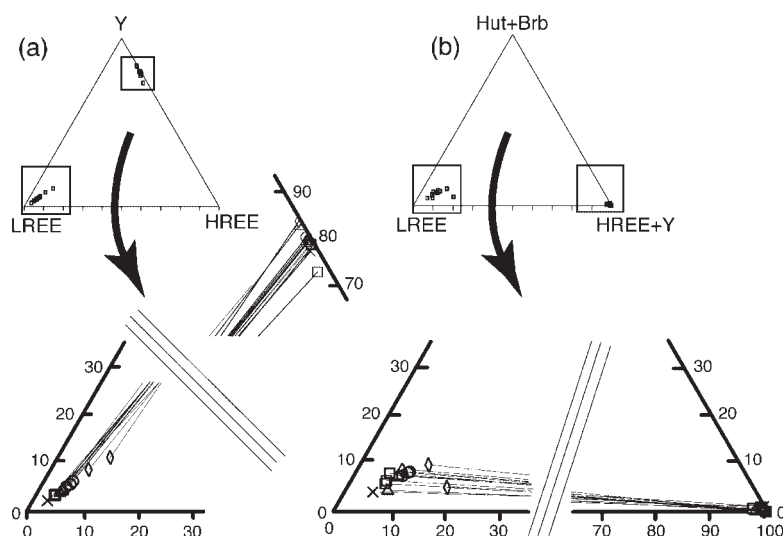


Fig. 5. Plots of coexisting monazite and xenotime. (a) Expanded LREEPO_4 – HREEPO_4 – YPO_4 ternary showing tie-lines between coexisting monazite and xenotime. (b) Expanded LREEPO_4 – $[\text{HREEPO}_4 + \text{YPO}_4]$ – $[\text{Ca}(\text{Th,U,Pb})(\text{PO}_4)_2 + (\text{Th,U,Pb})\text{SiO}_4]$ ternary. LREE, (La,Ce,Pr,Nd,Sm) PO_4 ; HREE, (Gd,Dy,Ho,Er,Yb) PO_4 ; Y, YPO_4 ; Hut, $\text{Ca}(\text{Th,U,Pb})(\text{PO}_4)_2$; Brb, $(\text{Th,U,Pb})\text{SiO}_4$; ×, biotite + chlorite zone; □, garnet zone; △, staurolite zone; ○, sillimanite zone; ◇, migmatite zone.

into growing monazite and garnet. On a modal (volumetric) basis, the (Y, HREE) uptake capacity of garnet is two or three orders of magnitude greater than that of monazite, but, at higher metamorphic grades, this uptake capacity of garnet for (Y, HREE) fractionation is counteracted by the lower solubility of (Y, HREE) in garnet (Pyle & Spear, 2000a).

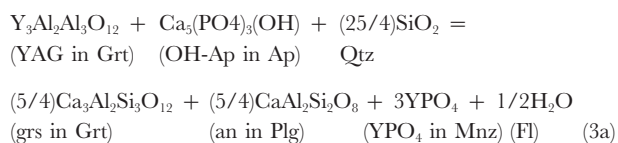
The inclusion of monazite in garnet is commonly taken as evidence that monazite was a stable phase during the period of garnet growth. Implicit in this assumption is that garnet and the included monazite are in compositional equilibrium. As element distribution maps clearly demonstrate, both garnet (Pyle & Spear, 1999) and monazite (Fig. 3) diffuse very slowly with respect to Y and HREE. Therefore, monazite included in garnet is not likely to re-equilibrate with trace components in garnet by diffusive exchange over geologically relevant time scales, except perhaps under extreme conditions of metamorphism. For practical purposes, monazite composition is ‘frozen’ once it is isolated from the matrix by surrounding garnet. Furthermore, the complex zoning observed in many monazite grains (e.g. Fig. 3) indicates that intragranular diffusion of Y and Th in monazite is slow.

The importance of understanding the reaction relationship between two refractory phases for assessing equilibrium coexistence based on textural criteria is illustrated in Fig. 10. Of the four possible reaction histories shown in the figure, the only combination that will yield coexisting equilibrium compositions is the first (both garnet and monazite grow). Most importantly, the presence of an included monazite in a garnet porphyroblast

such as illustrated in Fig. 10b does not assure two-phase equilibrium. This point illustrates that assumptions concerning equilibrium between porphyroblasts and included phases when both phases have extremely low diffusivities for the components of interest are prone to error without independent knowledge of the reaction relationship between the two phases of interest.

A new garnet–monazite thermometer

Some possible reactions describing mass transfer between YAG and xenotime were discussed by Pyle & Spear (2000a). For each of those reactions, an equivalent reaction can be written, replacing $\text{YPO}_4(\text{Xno})$ with $\text{YPO}_4(\text{Mnz})$. One possible reaction relating mass transfer between garnet and monazite involves consumption of YAG component of garnet, OH component of apatite, and quartz to produce grossular component of garnet, anorthite component of plagioclase, YPO_4 component of monazite, and a small amount of fluid:



with associated equilibrium constant

$$K_{\text{Eq}} = \frac{a_{\text{grs,Grt}}^{5/4} a_{\text{an,Plg}}^{5/4} a_{\text{YPO}_4\text{Mnz}}^3 f_{\text{H}_2\text{O}}^{1/2}}{a_{\text{YAG,Grt}} a_{\text{OH-AP,AP}}^{25/4} a_{\text{Qtz}}}. \quad (3b)$$

Assuming quartz is pure and single-site ionic ideal solution

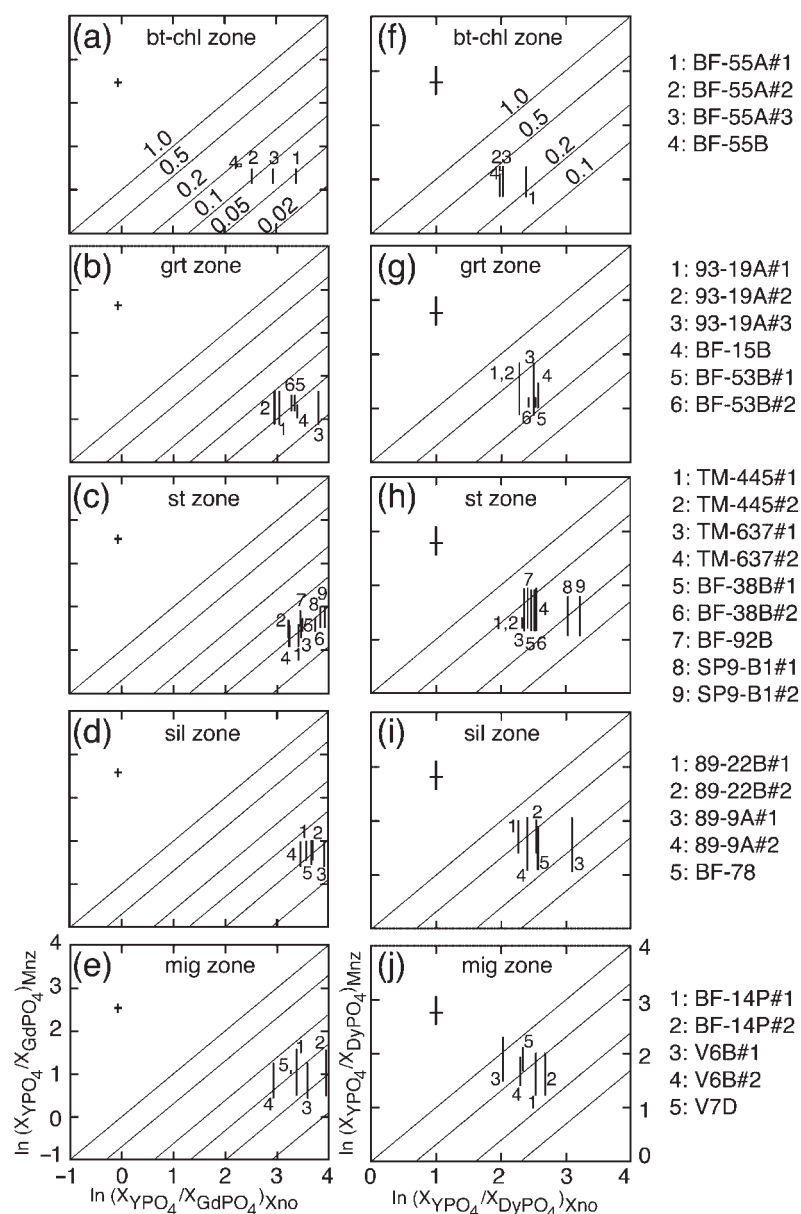


Fig. 6. Monazite–xenotime partitioning plots. (a–e) $\ln(\text{YPO}_4/\text{GdPO}_4)(\text{Mnz})$ vs $\ln(\text{YPO}_4/\text{GdPO}_4)(\text{Xno})$, and (f–j) $\ln(\text{YPO}_4/\text{DyPO}_4)(\text{Mnz})$ vs $\ln(\text{YPO}_4/\text{DyPO}_4)(\text{Xno})$ for (a, f) biotite + chlorite zone samples, (b, g) garnet zone samples, (c, h) staurolite zone samples, (d, i) sillimanite zone samples, and (e, j) migmatite zone samples. Plots represent partition coefficients for the total range of monazite compositions in a single sample, interpreted to be in equilibrium with xenotime, combined with 1–4 representative xenotime analyses per sample. Numbers on plots refer to sample numbers (see sidebar). Error bars represent propagation of analytical uncertainties (Bevington, 1969) in $X_{\text{YPO}_4, \text{Mnz}}$ (5%), $X_{\text{YPO}_4, \text{Xno}}$ (1%), $X_{\text{GdPO}_4, \text{Mnz}}$ (7.5%), $X_{\text{GdPO}_4, \text{Xno}}$ (5%), $X_{\text{DyPO}_4, \text{Mnz}}$ (25%), and $X_{\text{DyPO}_4, \text{Xno}}$ (5%). Diagonal lines are isopleths of K_D .

models for other phases, the equilibrium constant can be written as a function of composition:

$$K_{\text{Eq}} = \frac{X_{\text{Ca, Grt}}^{15/4} X_{\text{Ca, Plg}}^{5/4} X_{\text{Y, Mnz}}^3 f_{\text{H}_2\text{O}}^{1/2}}{X_{\text{Y, Grt}}^3 X_{\text{OH, AP}}} \quad (3c)$$

This equilibrium constant was calculated for 14 well-equilibrated garnet–monazite pairs (Table 9). The

selection of equilibrium monazite–garnet pairs is critical to the application of equilibrium relations in this system, and is fraught with potential pitfalls. In this study, the selection was based on element distribution maps of both phases combined with textural analysis and quantitative probe data. Additionally, Gibbs method modeling (e.g. Spear *et al.*, 1991) has been used to predict the growth

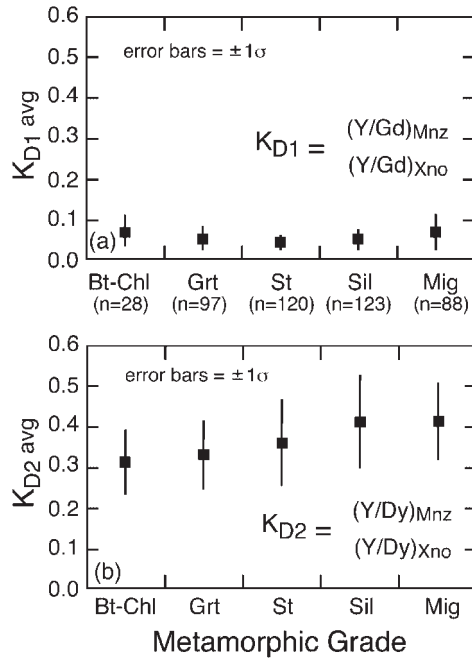


Fig. 7. Plots of (a) average K_{D1} and (b) K_{D2} vs metamorphic grade. $K_{D1} = (Y/Gd)_{Mnz}/(Y/Gd)_{Xno}$ and $K_{D2} = (Y/Dy)_{Mnz}/(Y/Dy)_{Xno}$. Bt-Chl, biotite–chlorite zone; Grt, garnet zone; St, staurolite zone; Sil, sillimanite zone; Mig, migmatite zone. Error bars represent ± 1 standard deviation on the average value of K_D for each metamorphic zone. Number of monazite analyses averaged per zone is given under the zone designation in part (a).

and/or consumption of garnet and accessory phases. Although the criteria for selection of equilibrium pairs are sample-specific, some general rules of thumb are given in Table 8. An additional, significant source of uncertainty arises from selection of plagioclase composition. In this study, garnet rim analyses were paired with the most albitic plagioclase in a particular sample, and garnet core analyses were paired with the highest anorthite content plagioclase in the sample. This is done under the assumption that in closed-system rocks without other calcic phases in significant abundance (i.e. Ca-carbonate or epidote), plagioclase becomes more albitic as garnet grows (Spear *et al.*, 1991); the extent to which consumption of apatite during garnet growth buffers X_{Grs} has not been studied.

Temperatures and pressures of equilibration were determined for each garnet–monazite pair (Pyle & Spear, 2000a). The fugacity of H_2O was calculated at P and T using the modified compensated Redlich–Kwong equation of Holland & Powell (1991), and the standard deviation of $f(H_2O)$ was calculated with a Monte Carlo simulation consisting of 1000 trials. Variations in $f(H_2O)$ (an explicit function of P and T) also have only a small effect on the calculated equilibrium constant; changing

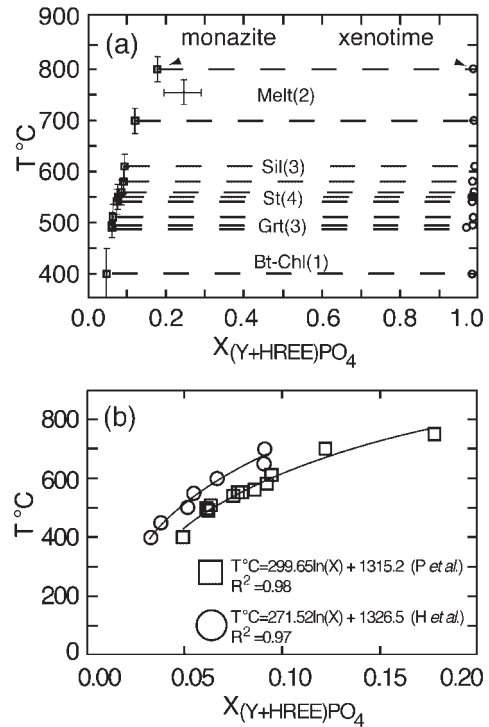


Fig. 8. (a) Temperature vs $X_{(HREEPO_4 + YPO_4)}$ for coexisting monazite (\square) and xenotime (\circ). Temperature estimates from garnet–biotite thermometry (Hodges & Spear, 1982) and YAG–xenotime thermometry (Pyle & Spear, 2000a). Vertical error bars indicate $\pm 25^\circ\text{C}$ ($\pm 50^\circ\text{C}$ for the lowest grade sample) and horizontal error bars indicate ± 5 mol %. (b) Enlargement of (a) showing detail of monazite compositions. Monazite limb (continuous line with \square ; P *et al.*) is a logarithmic fit to the data from this study. Monazite limb from Heinrich *et al.* (1997; H *et al.*) with associated logarithmic fit is plotted for comparison.

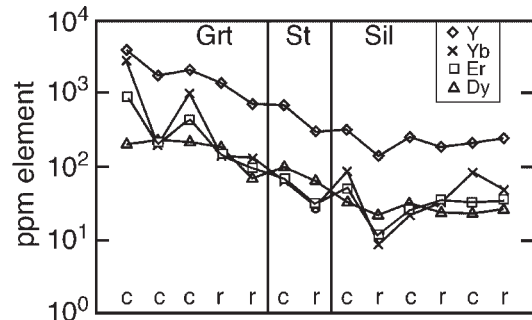


Fig. 9. Plot of Y and selected HREE (Yb, Er, Dy) concentration in garnet vs metamorphic grade for garnet coexisting with xenotime. \diamond , Y; \times , Yb; gray squares, Er; \triangle , Dy. Grt, garnet zone; St, staurolite zone; Sil, sillimanite zone; c, core analyses; r, rim analyses. Analyses ordered by metamorphic grade and by position (core vs rim).

the input value of $f(H_2O)$ by ± 1000 results in a ΔT of $\pm 3^\circ\text{C}$. The volume of YPO_4 monazite was calculated using the linear regression of Ni *et al.* (1995). ΔV_{rxn} for

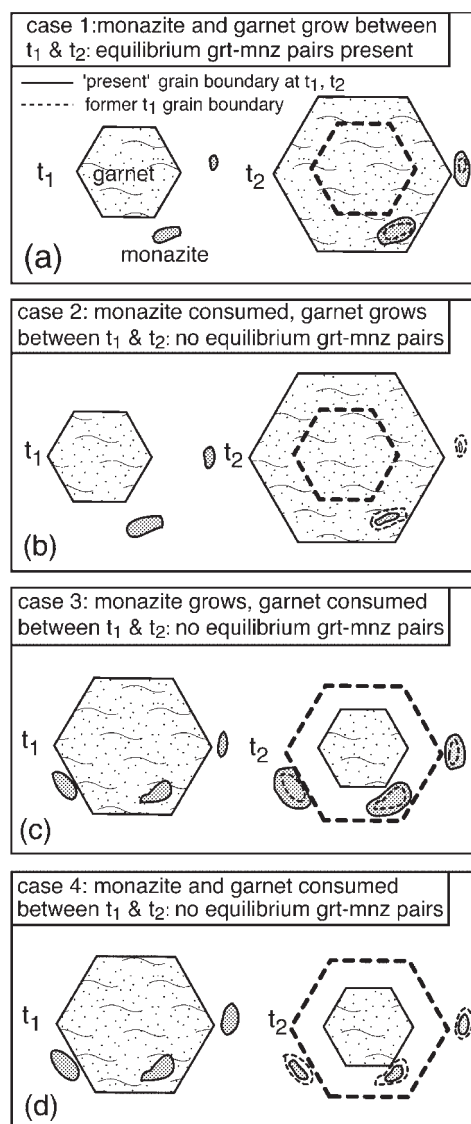


Fig. 10. Schematic representation of the possible combinations of garnet and monazite reaction relationships and the implications of these for finding equilibrated garnet–monazite pairs. Left: continuous outlines show grain boundary positions at time 1 (t_1). Right: continuous lines show grain positions at time 2 (t_2), and dashed lines show former (t_1) grain boundary positions. Garnet and monazite are assumed to be in equilibrium at t_1 , and both are assumed to be refractory (zoned) phases. (a) Garnet and monazite both grow between t_1 and t_2 . The grain boundary of included monazite is in equilibrium with some portion of the occluding garnet between the monazite–garnet grain boundary and the garnet–matrix grain boundary. Rim of matrix monazite is in equilibrium with rim of garnet. (b) Garnet grows and monazite is consumed between t_1 and t_2 . (c) Garnet is consumed and monazite grows between t_1 and t_2 . (d) Garnet and monazite both consumed between t_1 and t_2 . In (b), (c), and (d), no existing portion of garnet is in equilibrium with monazite.

(3a) varies from -1.28 J/bar (BF-78) to -1.61 J/bar (V7C) over the P – T range of the samples (450–800°C, 3–8 kbar).

Values of $\ln(K_{\text{Eq}}) + P\Delta V/RT$ for equilibrium garnet–monazite pairs (Table 9) were regressed against reciprocal temperature (Fig. 11). The goodness of fit ($R^2 = 0.94$) shown in Fig. 11 suggests that there is a systematic relationship between YAG component of garnet and $\text{YPO}_4(\text{Mnz})$ over the range of temperatures examined. Assuming $\Delta C_p = 0$, the least-squares fit to the data yields values of $\Delta H_{\text{rxn}} = 447.8 (\pm 32.1)$ kJ and $\Delta S_{\text{rxn}} = 0.57 (\pm 0.04)$ kJ/K. The Clausius–Clapeyron relation yields dP/dT estimates of ~ 345 – 425 bars/°C for reaction (3a) over the P – T range studied.

Importantly, the systematic relationship between YAG and $\text{YPO}_4(\text{Mnz})$ appears to hold for xenotime-absent samples as well. Textural and compositional analysis of samples PUT-92C2 (garnet zone), BF-17 and BF-52 (staurolite zone), and V7C (migmatite zone) indicates that some garnet growth in each of these samples occurred in a xenotime-absent assemblage. Monazite grains texturally associated with these low-Y garnets are depleted in yttrium compared with monazite texturally associated with xenotime. Values of $\ln(K_{\text{Eq}}) + P\Delta V/RT$ for these four samples (open squares, Fig. 11) fall on the trend defined by $\ln(K_{\text{Eq}})$ for xenotime-bearing samples, suggesting that equilibrium between garnet and monazite is achieved by a significant decrease in both YAG and $\text{YPO}_4(\text{Mnz})$.

A YAG–monazite geothermometer using derived values of ΔH and ΔS for reaction (3a) relates temperature and $\ln(K_{\text{Eq}})$ via

$$T(^{\circ}\text{C}) = \left(\frac{-1.45P(\text{bars}) + 447772(\pm 32052)}{567(\pm 40) - R\ln(K_{\text{Eq}})} \right) - 273.15 \quad (4)$$

where -1.45 is an average value of ΔV_{rxn3a} (J/bar), and $R = 8.314$ J/mol K. Propagation of uncertainties in P (± 1000 bars), ΔV (1%), ΔH , ΔS , and $\ln(K_{\text{Eq}})$ results in temperature uncertainties of roughly ± 20 – 30°C for all samples. However, these temperature uncertainties were propagated using typical electron microprobe analytical uncertainties (± 1 mol % for major components, ± 0.1 % for YAG), and application of more accurate and/or precise analytical tools (LA-ICP-MS, ion probe) would reduce the propagated temperature uncertainty considerably.

Another potential source of error lies in assumptions of fluid composition. The calibration presented here assumes a pure H_2O fluid, but other components (CO_2 , F, Cl) are likely to be present to some extent. However, the amount of fluid involved in reaction (3a) is small, and errors in estimation of fluid composition affect the calculated temperature only to a small degree; assumption of a pure H_2O fluid where the true fluid composition is $X_{\text{H}_2\text{O}} = 0.1$ results in a temperature error of only $\pm 2^{\circ}\text{C}$, an order of magnitude less than the precision associated

Table 8: Ranked textural and compositional criteria for assumption of monazite–garnet compositional equilibrium

Observed textural and/or compositional criteria	Assumption	Relative rank
Inclusion of homogeneous monazite in homogeneous or continuously Y-zoned garnet	Both grains in (compositional) equilibrium	1
Discontinuously Y-zoned monazite included in homogeneous or continuously Y-zoned garnet	Garnet in equilibrium with outer portion of monazite	2
Matrix monazite and garnet both homogeneous or continuously Y-zoned	Both grains in equilibrium	3
Garnet homogeneous or continuously Y-zoned; matrix monazite discontinuously Y-zoned	Garnet in equilibrium with outer portion of monazite	4
Garnet discontinuously Y-zoned, included monazite discontinuously Y-zoned	None: knowledge of reaction relationship needed	—
Garnet discontinuously Y-zoned; matrix monazite discontinuously Y-zoned	None: knowledge of reaction relationship needed	—
Textural evidence for monazite–garnet reaction relationship	Monazite and portion of garnet involved in reaction in equilibrium if reaction produces both phases	Used in conjunction with all of above

with compositional uncertainties. In addition, isopleths of K_{Eq} in P – T space (Fig. 12) are virtually linear above low confining pressures, as a result of the small amount of fluid evolved in reaction (3a).

Application of the YAG–monazite thermometer

The application of the YAG–monazite thermometer to a sample with multistage monazite growth history is presented for sample BF-58, a staurolite-zone schist from north of Bellows Falls, VT, USA. The sample contains garnet discontinuously zoned in yttrium (Fig. 13a), with core composition of $X_{\text{YAG}} = 0.0045$ (~ 2450 ppm Y) and rim composition of $X_{\text{YAG}} = 0.00012$ (68 ppm Y). Monazite is bimodally zoned in yttrium (Fig. 13b and c) with cores of $X_{\text{YPO}_4} = 0.0325$ and rims of $X_{\text{YPO}_4} = 0.0092$. Matrix plagioclase composition averages An_{6-7} , and apatite inclusions in garnet have $X_{\text{OH-Ap}} = 0.33$, in contrast to matrix apatite ($X_{\text{OH-Ap}} = 0.11$).

Mass balance considerations and Gibbs method modeling (Pyle & Spear, 2000b) reveal that during prograde metamorphism of pelites, xenotime-bearing assemblages experience monazite growth and xenotime consumption simultaneous with $\text{Chl} + \text{Qtz} = \text{Grt} + \text{Fl}$. Upon loss of xenotime from the mineral assemblage, monazite is consumed during further garnet growth. At the staurolite isograd ($\text{Grt} + \text{Chl} = \text{St} + \text{Bt}$), a second episode of

monazite growth is initiated (along with xenotime if sufficient Y is present), and monazite continues to grow along with garnet during the divariant (in KFMASH) $\text{Grt} + \text{Bt} = \text{St} + \text{Ms}$ reaction ($\text{St} + \text{Ms} = \text{Grt} + \text{Bt}$). Thus, garnet cores are interpreted to be in equilibrium with high-Y monazite in an early Y-rich (xenotime-bearing?) assemblage. The garnet rims are interpreted to be in equilibrium with low-Y monazite rims, representing the xenotime-absent, post-staurolite isograd reaction assemblage. Apatite inclusions in garnet are paired with the early (garnet core–monazite core) assemblage, and matrix apatite with the rims of garnet and monazite. Assuming a value of $f_{\text{H}_2\text{O}}^{1/2} = 40$, and plagioclase composition of An_7 , application of the YAG–monazite thermometer yields a garnet core temperature estimate of $463 \pm 20^\circ\text{C}$, and a garnet-rim (staurolite zone) temperature estimate of $541 \pm 20^\circ\text{C}$ (both at $P = 4$ kbar).

These temperature estimates agree well with other thermometry estimates from these rocks (Spear *et al.*, 1990), but, more importantly, demonstrate that garnet and monazite maintain compositional equilibrium even as garnet fractionation drastically changes the effective Y bulk composition of the sample. The change in composition between included and matrix apatite indicates that pelitic apatite also evolves compositionally during prograde metamorphism; pairing of included apatite

Table 9: Values used in regression of YAG–monazite thermometer

Sample:	BF-17	BF-17	BF-17	BF-15	TM-549	BF-15	93-19	PUT	BF-52	TM-445	TM-637	BF-38	89-9	89-22	BF-78	V7C
X _{no?}	Y	N	N	Y	Y	Y	Y	N	N	Y	Y	Y	Y	Y	Y	N
X _{grs}	0.070	0.120	0.083	0.043	0.043	0.043	0.043	0.030	0.060	0.0650	0.070	0.051	0.039	0.065	0.029	0.062
X _{YAG}	0.0097	0.00037	0.0074	0.0037	0.0037	0.0037	0.0039	0.0004	0.0003	0.0011	0.0003	0.00056	0.0010	0.0004	0.4	0.00003
X _{grt}	0.03	0.03	0.21	0.05	0.05	0.05	0.15	0.15	0.20	0.20	0.10	0.20	0.24	0.20	0.25	0.50
X _{PO4}	0.0225	0.0076	0.0206	0.0319	0.0295	0.0295	0.0295	0.0038	0.0066	0.0410	0.0306	0.03313	0.0539	0.0488	0.0596	0.0098
X _{OH-Ap}	0.270	0.076	0.210	0.016	0.051	0.051	0.051	0.016	0.195	0.160	0.265	0.233	0.244	0.166	0.260	0.280
f(H ₂ O)	1262.7	1631.1	1931.4	1516.2	1387.1	1452.4	1452.4	1452.4	1631.1	4582.5	3428.7	2445.5	1443.8	1446.6	1472.9	1520.8
ln(K _{eq})	-6.936	3.064	-2.807	-1.281	-1.504	-1.269	-1.269	-1.269	2.021	4.667	6.504	4.427	3.062	5.224	6.512	13.19
P	4000	4000	5000	4000	3800	4000	4000	4000	4000	7000	6000	5000	3000	3000	2800	8000
T	400	450	480	500	495	490	490	525	525	550	550	540	530	580	610	700
Grt	core	rim	core	rim	rim	rim	rim	rim	rim	rim	rim	rim	core	rim	core	rim
Ap	incl	mxtr	mxtr	mxtr	mxtr	mxtr	mxtr	mxtr	mxtr	mxtr	mxtr	mxtr	incl	mxtr	incl	mxtr

Y, xenotime present in assemblage; N, xenotime absent from assemblage; P, pressure in kbar; T, temperature in °C; core, garnet core analysis; rim, garnet rim analysis; incl, apatite inclusion in garnet; mxtr, matrix apatite.

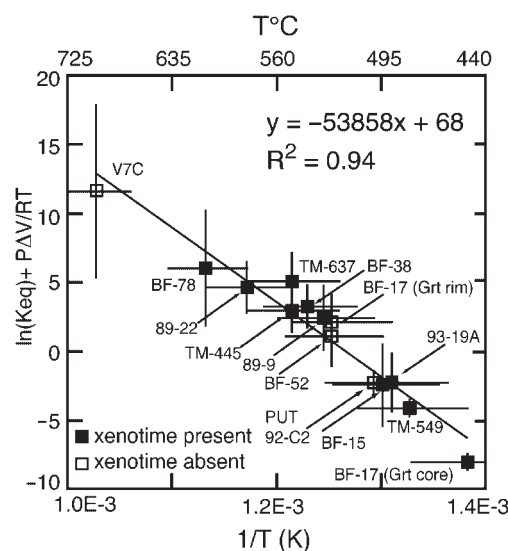


Fig. 11. Plot of $\ln(K_{eq}) + P\Delta V/RT$ vs reciprocal temperature for the reaction $YAG + OH\text{-apatite} + (25/4)\text{quartz} = (5/4)\text{grossular} + (5/4)\text{anorthite} + 3YPO_4(\text{monazite}) + 1/2H_2O$ [reaction (3a)]. ■, xenotime-bearing assemblages; □, xenotime-absent assemblages. Least-squares regression line is fitted to all data points. Horizontal error bars represent temperature uncertainty of $\pm 30^\circ\text{C}$. Vertical error bars are $\pm 1\sigma [\ln(K_{eq}) + P\Delta V/RT]$, derived from propagation of uncertainties in P (± 1000 bars), T ($\pm 30^\circ\text{C}$), ΔV_{rxn} (1%), compositional parameters (0.001 mole fraction YAG, 0.01 mole fraction all others), and $f(H_2O)$ (± 7.5 ; 1000 trial Monte Carlo simulation). Labels on graph indicate sample numbers.

($X_{OH} = 0.33$) with rim garnet and monazite introduces variation in temperature estimation of the same order as the propagated T uncertainty (i.e. $\pm 16^\circ\text{C}$).

CONCLUSIONS

Monazite compositional zoning records multiple reaction events in a rock. This study demonstrates that monazite is not an inert temporal marker, but rather participates in reactions involving both accessory and major phases. The textural and compositional evidence presented in this paper shows that monazite composition is, in part, controlled by the major-phase mineral assemblage, and, hence, the reactions that produce and consume major phases.

Throughout a prograde metamorphic sequence, monazite approaches compositional equilibrium with both accessory phases (e.g. xenotime) and trace components of major phases (e.g. YAG in garnet), as shown by (1) consistency of elemental partitioning, and (2) systematic behavior of the equilibrium constant in coupled major-accessory phase net-transfer reactions. This demonstration of a close approach to compositional equilibrium has applications for both accessory-phase only

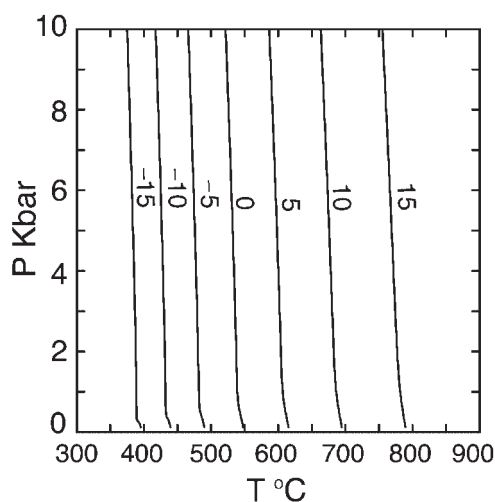


Fig. 12. P – T plot contoured with isopleths of $\ln(K_{Eq})$ for reaction (3a). Reaction (3a) evolves very little fluid on a molar basis, and the resulting isopleths are virtually linear except at very low ($P < 500$ bars) pressures. dP/dT of $\ln(K_{Eq})$ varies from ~ 345 to 425 bars/ $^{\circ}\text{C}$ over the P – T range studied.

geothermometry, and major phase–accessory phase geothermometry.

The importance of the detailed textural analysis combined with element distribution maps in a study such as this cannot be overstated. Selection of ‘equilibrium’ pairs of minerals requires careful investigation, and element distribution maps are required to reveal the complexity of a sample’s reaction history. Methods outlined above can be used to identify mineral pairs that represent part of an equilibrium mineral assemblage. Correlation of monazite growth with major phase growth and P – T path allows the dating of specific points along a P – T path, and allows for calculation of heating and loading rates.

ACKNOWLEDGEMENTS

We thank David A. Wark and Kiera Becker for analytical support and maintenance of the JEOL 733 Superprobe at Rensselaer Polytechnic Institute. Ingo Horn and Jarek Labziewicz are also thanked for their assistance with LA-ICP-MS analyses and data reduction at the Department of Earth and Planetary Sciences, Harvard University. This study was funded by NSF grants EAR-9706463 and EAR-9903036 to F.S.S., and EAR-9711088 and EAR-9726058 to R.L.R. and W.F.M. Constructive, in-depth reviews by Gavin Foster, Jean-Marc Montel and Randy Parrish significantly improved the final version. Simon Harley is also thanked for his editorial handling of the manuscript.

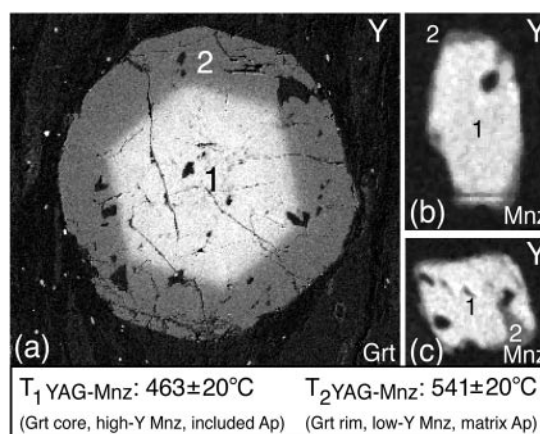


Fig. 13. Yttrium distribution maps of garnet (a) and matrix monazite (b, c) in staurolite-zone sample BF-58. Garnet contains Y-enriched (~ 2450 ppm) core and Y-poor (~ 65 ppm) rim. Matrix monazites are also discontinuously zoned in Y (~ 1.5 wt % Y_2O_3 core, ~ 0.7 wt % Y_2O_3 rim). Monazite ‘1’ grew in the assemblage Grt + Bt + Chl + Xno, whereas monazite ‘2’ grew in the assemblage Grt + Bt + St \pm Chl (xenotime-absent). YAG–monazite thermometry pairing garnet and monazite ‘1’ with apatite included in garnet ($X_{\text{OHAp}} = 0.33$) yields a low-garnet-zone temperature estimate ($463 \pm 20^{\circ}\text{C}$); garnet + monazite ‘2’ paired with matrix apatite (garnet ($X_{\text{OHAp}} = 0.10$) yields a high-garnet-zone or staurolite-zone temperature estimate ($541 \pm 20^{\circ}\text{C}$).

REFERENCES

- Andrehs, G. & Heinrich, W. (1998). Experimental determination of REE distributions between monazite and xenotime: potential for temperature-calibrated geochronology. *Chemical Geology* **149**, 83–96.
- Armstrong, J. T. (1984). Quantitative analysis of silicate and oxide minerals: a reevaluation of ZAF corrections and proposal for new Bence–Albee coefficients. In: Romig, A. D. & Goldstein, J. I. (eds) *Microbeam Analysis*. San Francisco Press, **19**, 208–212.
- Ayers, J. C., Miller, C., Gorisch, B. & Milleman, J. (1999). Textural development of monazite during high-grade metamorphism: hydrothermal growth kinetics, with implications for U, Th–Pb geochronology. *American Mineralogist* **84**, 1766–1780.
- Barth, M. G., Rudnick, R. L., Horn, I., McDonough, W. F., Spicuzza, M. J., Valley, J. W. & Haggerty, S. E. (2001). Geochemistry of xenolithic eclogites from West Africa, part I: a link between low MgO eclogites and Archean crust formation. *Geochimica et Cosmochimica Acta* **65**, 1499–1527.
- Bea, F. (1996). Residence of REE, Y, Th, and U in granites and crustal protoliths; implications for the chemistry of crustal melts. *Journal of Petrology* **37**, 521–552.
- Bea, F., Pereira, M. D. & Stroh, A. (1994). Mineral/leucosome partitioning in a peraluminous migmatite (a laser ablation-ICP-MS study). *Chemical Geology* **117**, 291–312.
- Beverington, P. R. (1969). *Data Reduction and Error Analysis for the Physical Sciences*. New York: McGraw–Hill.
- Bingen, B., Demaiffe, D. & Hertogen, J. (1996). Redistribution of rare earth elements, thorium, and uranium over accessory minerals in the course of amphibolite to granulite facies metamorphism: the role of apatite and monazite in orthogneisses from southwestern Norway. *Geochimica et Cosmochimica Acta* **60**, 1341–1354.
- Broska, I. & Siman, P. (1998). The breakdown of monazite in the West-Carpathian Veporic orthogneisses and Tatric granites. *Geologica Carpathica* **49**, 161–167.

- Crowley, J. L. & Ghent, E. D. (1999). An electron microprobe study of the U–Pb–Th systematics of metamorphosed monazite: the role of Pb diffusion versus overgrowth and recrystallization. *Chemical Geology* **157**, 285–302.
- Cruft, E. F. (1966). Minor elements in igneous and metamorphic apatite. *Geochimica et Cosmochimica Acta* **30**, 375–398.
- Ferry, J. M. (2000). Patterns of mineral occurrence in metamorphic rock. *American Mineralogist* **85**, 1573–1588.
- Finger, F., Broska, I., Roberts, M. P. & Schermaier, A. (1998). Replacement of primary monazite by apatite–allanite–epidote coronas in an amphibolite facies granite gneiss from the eastern Alps. *American Mineralogist* **83**, 248–258.
- Förster, H.-J. (1998). The chemical composition of REE–Y–Th–U-rich accessory minerals in peraluminous granites in the Erzgebirge–Fichtelgebirge region, Germany, part I: the monazite–(Ce)–brabantite solid solution series. *American Mineralogist* **83**, 258–272.
- Foster, G., Kinny, P., Vance, D., Prince, C. & Harris, N. (2000). The significance of monazite U–Th–Pb age data in metamorphic assemblages; a combined study of monazite and garnet chronometry. *Earth and Planetary Science Letters* **181**, 327–340.
- Franz, G., Andrehs, D. & Rhede, G. (1996). Crystal chemistry of monazite and xenotime from Saxothuringian–Moldanubian metapelites, NE Bavaria, Germany. *European Journal of Mineralogy* **8**, 1097–1118.
- Gratz, R. & Heinrich, W. (1997). Monazite–xenotime thermobarometry: experimental calibration of the miscibility gap in the system CePO_4 – YPO_4 . *American Mineralogist* **82**, 772–780.
- Gratz, R. & Heinrich, W. (1998). Monazite–xenotime thermometry, III; experimental calibration of the partitioning of gadolinium between monazite and xenotime. *European Journal of Mineralogy* **10**, 579–588.
- Harrison, T. M., Ryerson, F. J., Le Fort, P., Yin, A., Lovera, O. M. & Catlos, E. J. (1997). A Late Miocene–Pliocene origin for the Central Himalayan inverted metamorphism. *Earth and Planetary Science Letters* **146**, 1–7.
- Hawkins, D. P. & Bowring, S. A. (1999). U–Pb monazite, xenotime and titanite geochronological constraints on the prograde to post-peak metamorphic thermal history of Paleoproterozoic migmatites from the Grand Canyon, Arizona. *Contributions to Mineralogy and Petrology* **134**, 150–169.
- Heinrich, W., Andrehs, G. & Franz, G. (1997). Monazite–xenotime miscibility gap thermometry. I. An empirical calibration. *Journal of Metamorphic Geology* **15**, 3–16.
- Holland, T. & Powell, R. (1991). A compensated Redlich–Kwong (CORK) equation for volumes and fugacities of CO_2 and H_2O in the range 1 bar to 50 kbar and 100–1600°C. *Contributions to Mineralogy and Petrology* **109**, 265–273.
- Horn, I., Rudnick, R. L. & McDonough, W. F. (2000). Precise elemental and isotope ratio determination by simultaneous solution nebulization and laser ablation–ICP–MS; application to U–Pb geochronology. *Chemical Geology* **164**, 281–301.
- Kohn, M. J. & Spear, F. S. (1991). Error propagation for barometers: 2. Application to rocks. *American Mineralogist* **76**, 138–147.
- Kohn, M. J., Spear, F. S. & Dalziel, I. W. D. (1993). Metamorphic P – T paths from Cordillera Darwin, a core complex in Tierra del Fuego, Chile. *Journal of Petrology* **34**, 519–542.
- Kohn, M. J., Spear, F. S. & Valley, J. W. (1997). Dehydration–melting and fluid recycling during metamorphism: Rangeley Formation, New Hampshire, USA. *Journal of Petrology* **38**, 1255–1277.
- Kretz, R. (1983). Symbols for rock-forming minerals. *American Mineralogist* **68**, 277–279.
- Kretz, R., Campbell, J. L., Hoffman, E. L., Hartree, R. & Teesdale, W. J. (1999). Approaches to equilibrium in the distribution of trace elements among the principal minerals in a high-grade metamorphic terrane. *Journal of Metamorphic Geology* **17**, 41–59.
- Longerich, H. P., Jackson, S. E. & Günther, D. (1996). Laser ablation inductively coupled plasma mass spectrometric transient signal data acquisition and analyte concentration calculation. *Journal of Analytical Atomic Spectrometry* **11**, 899–904.
- Menard, T. & Spear, F. S. (1993). Metamorphism of calcic pelitic schists, Stratford Dome, Vermont: compositional zoning and reaction history. *Journal of Petrology* **34**, 977–1005.
- Menard, T. & Spear, F. S. (1994). Metamorphic P – T paths from calcic pelitic schists from the Stratford Dome, Vermont, USA. *Journal of Metamorphic Geology* **12**, 811–826.
- Montel, J. M., Veschambre, M. & Nicollet, C. (1994). Datation de la monazite à la microsonde électronique. *Comptes Rendus de l'Académie des Sciences, Série II*, **318**, 1489–1495.
- Montel, J. M., Foret, S., Veschambre, M., Nicollet, C. & Provost, A. (1996). Electron microprobe dating of monazite. *Chemical Geology* **131**, 37–53.
- Ni, Y., Hughes, J. M. & Mariano, A. N. (1995). Crystal chemistry of the monazite and xenotime structures. *American Mineralogist* **80**, 21–26.
- Pan, Y. (1997). Zircon- and monazite-forming reactions at Manitouwadge, Ontario. *Canadian Mineralogist* **35**, 105–118.
- Parrish, R. R. (1990). U–Pb dating of monazite and its application to geological problems. *Canadian Journal of Earth Sciences* **27**, 1431–1450.
- Poirasson, F., Chenery, S. & Bland, D. J. (1996). Contrasted monazite hydrothermal alteration mechanisms and their geological implications. *Earth and Planetary Science Letters* **145**, 79–96.
- Pyle, J. M. & Spear, F. S. (1999). Yttrium zoning in garnet: coupling of major and accessory phases during metamorphic reactions. *Geological Materials Research* **1**(6), 1–49.
- Pyle, J. M. & Spear, F. S. (2000a). An empirical garnet (YAG)–xenotime thermometer. *Contributions to Mineralogy and Petrology* **138**, 51–58.
- Pyle, J. M. & Spear, F. S. (2000b). Accessory-phase paragenesis in low- P migmatites, Chesham Pond nappe, SE New Hampshire. *Geological Society of America Annual Meeting, Abstracts with Programs* **32**, A297.
- Reed, S. J. B. & Buckley, A. (1996). Virtual WDS. *Mikrochimica Acta* **13**, 479–483.
- Scherer, N. C., Engi, M., Gnoss, E., Jakob, V. & Leichti, A. (2000). Monazite analysis; from sample preparation to microprobe age dating and REE quantification. *Schweizerische Mineralogische und Petrographische Mitteilungen* **80**, 93–105.
- Spear, F. S. (1992). Inverted metamorphism, P – T paths, and the cooling history of west-central New Hampshire: implications for the tectonic evolution of central New England. In: Robinson, P. & Brady, J. (eds) *Guidebook for Fieldtrips in the Connecticut Valley Region of Massachusetts and the Adjacent States*. Amherst, MA: Department of Geology and Geography, University of Massachusetts, pp. 446–466.
- Spear, F. S. & Kohn, M. J. (1996). Trace element zoning in garnet as a monitor of crustal melting. *Geology* **24**, 1099–1102.
- Spear, F. S. & Parrish, R. R. (1996). Petrology and cooling rates of the Valhalla Complex, British Columbia, Canada. *Journal of Petrology* **37**, 733–763.
- Spear, F. S., Hickmott, D. D. & Selverstone, J. (1990). Metamorphic consequences of thrust emplacement, Fall Mountain, New Hampshire. *Geological Society of America Bulletin* **102**, 1344–1360.
- Spear, F. S., Kohn, M. J., Florence, F. P. & Menard, T. (1991). A model for garnet and plagioclase growth in pelitic schists: implications for thermobarometry and P – T path determinations. *Journal of Metamorphic Geology* **8**, 683–696.
- Spear, F. S., Kohn, M. J. & Paetzold, S. (1995). Petrology of the regional sillimanite zone, west-central New Hampshire, U.S.A., with implications for the development of inverted isograds. *American Mineralogist* **80**, 361–376.

- Stormer, J. C., Jr, Pierson, M. J. & Tacker, R. C. (1993). Variation of F and Cl X-ray intensity due to anisotropic diffusion of apatite during electron microprobe analysis. *American Mineralogist* **78**, 641–648.
- Suzuki, K. & Adachi, M. (1991). Precambrian provenance and Silurian metamorphism of the Tsubonosawa paragneiss in the South Kitakami Terrane, northeast Japan, revealed by the chemical Th–U–Total Pb isochron ages of monazite, zircon and xenotime. *Geochemical Journal* **25**, 357–376.
- Wark, D. A. & Miller, C. L. (1993). Accessory mineral behavior during differentiation of a granite suite: monazite, xenotime and zircon in the Sweetwater Wash pluton, southeastern California, U.S.A *Chemical Geology* **110**, 49–67.
- Watson, E. B., Cherniak, D. J., Hanchar, J. M., Harrison, T. M. & Wark, D. A. (1997). The incorporation of Pb into zircon. *Chemical Geology* **141**, 19–31.
- Watt, G. L. & Harley, S. L. (1993). Accessory phase controls on the geochemistry of crustal melts and restites produced during water-undersaturated partial melting. *Contributions to Mineralogy and Petrology* **114**, 550–566.
- Watt, G. R. (1995). High-thorium monazite-(Ce) formed during disequilibrium melting of metapelites under granulite-facies conditions. *Mineralogical Magazine* **59**, 735–743.
- Williams, M. L., Jercinovic, M. J. & Terry, M. P. (1999). Age mapping and dating of monazite on the electron microprobe; deconvoluting multistage tectonic histories. *Geology* **27**, 1023–1026.
- Yan, X.-U., Kerrich, R. & Hendry, M. J. (2000). Trace element geochemistry of a thick till and clay-rich aquitard sequence, Saskatchewan, Canada. *Chemical Geology* **164**, 93–120.
- Yang, P. & Rivers, T. (2000). Trace element partitioning between coexisting biotite and muscovite from metamorphic rocks, western Labrador: structural, compositional and thermal controls. *Geochimica et Cosmochimica Acta* **64**, 1451–1472.
- Yang, P., Rivers, T. & Jackson, S. (1999). Crystal-chemical and thermal controls on trace-element partitioning between coexisting garnet and biotite in metamorphic rocks from western Labrador. *Canadian Mineralogist* **37**, 443–468.
- Zhu, X. K. & O’Nions, R. K. (1999a). Zonation of monazite in metamorphic rocks and its implications for high temperature thermochronology: a case study from the Lewisian terrain. *Earth and Planetary Science Letters* **171**, 209–220.

Zhu, X. K. & O’Nions, R. K. (1999b). Monazite chemical composition: some implications for monazite geochronology. *Contributions to Mineralogy and Petrology* **137**, 351–363.

Ziebold, T. (1967). Precision and sensitivity in electron microprobe analysis. *Analytical Chemistry* **39**, 858–861.

APPENDIX: MOLE FRACTION CALCULATIONS

The mole fractions for components in monazite and xenotime were calculated with the following equations.

Mole fraction $A_i\text{PO}_4$, where A_i = La, Ce, Sm, Pr, Nd, Gd, Dy, Yb, Er, Ho, Y:

$$X_{A_i\text{PO}_4} = A_i/D. \quad (\text{A1})$$

Mole fraction brabantite (brb) [where brabantite formula is $\text{Ca}(\text{Th,U,Pb})(\text{PO}_4)_2$] (note that Pb is included with U and Th, because it is assumed that all Pb is radiogenic):

$$X_{\text{brb}} = (2\text{Ca})/D. \quad (\text{A2})$$

Mole fraction huttonite (hut) [where huttonite formula is $(\text{Th,U,Pb})\text{SiO}_4$] (note that Pb is included with U and Th, because it is assumed that all Pb is radiogenic):

$$X_{\text{hut}} = (\text{Th} + \text{U} + \text{Pb} - \text{Ca})/D \quad (\text{A3})$$

where $D = [\text{La} + \text{Ce} + \text{Sm} + \text{Pr} + \text{Nd} + \text{Gd} + \text{Dy} + \text{Yb} + \text{Er} + \text{Ho} + \text{Y} + (2\text{Ca}) + (\text{Th} + \text{U} + \text{Pb} - \text{Ca})]$

$$X_{\text{LREE}} = X_{\text{LaPO}_4} + X_{\text{CePO}_4} + X_{\text{PrPO}_4} + X_{\text{NdPO}_4} + X_{\text{SmPO}_4}$$

$$X_{\text{HREE}} = X_{\text{GdPO}_4} + X_{\text{DyPO}_4} + X_{\text{HoPO}_4} + X_{\text{ErPO}_4} + X_{\text{YbPO}_4}.$$